



Linear friction welding of AD730™ Ni-base superalloy: Process-microstructure-property interactions

F. Masoumi ^{a,*}, D. Shahriari ^a, H. Monajati ^a, J. Cormier ^b, B.C.D. Flipo ^c, A. Devaux ^d, M. Jahazi ^{a,*}

^a Department of Mechanical Engineering, École de Technologie Supérieure (ÉTS), Montreal, QC H3C 1K3, Canada

^b Institute Pprime, UPR CNRS 3346, Physics and Mechanics of Materials Department, ISAE, ENSMA, BP 40109, Futuroscope, Chasseneuil Cedex 86961, France

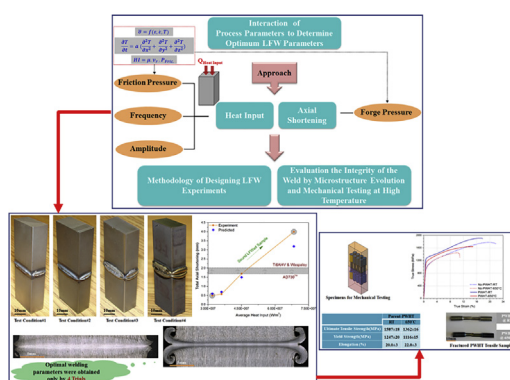
^c TWI Ltd, Granta Park, Great Abington, Cambridge CB21 6AL, UK

^d Aubert & Duval, Site des Ancizes, BP1, 63770 Les Ancizes Cedex, France

HIGHLIGHTS

- Analytical method is proposed to obtain LFW process parameters of AD730™ alloy and have a sound weld with minimum trials.
- Microstructure evolution and mechanical properties as a function of LFW parameters are studied to confirm the approach.
- The fracture mechanisms of the as-welded and suggested post-weld heat treated samples during tensile tests are analyzed.

GRAPHICAL ABSTRACT



ARTICLE INFO

Article history:

Received 17 June 2019

Received in revised form

5 August 2019

Accepted 10 August 2019

Available online 13 August 2019

Keywords:

AD730™ Ni-base superalloy

Linear friction welding

Process parameter

Analytical method

Microstructure

Mechanical property

ABSTRACT

Linear friction welding (LFW) is a near net shape solid state joining technology for aerospace applications. In this study LFW of a recently introduced Ni-based superalloy, AD730™, with superior properties for use in the hot section of gas turbines was studied. In order to minimize the number of experiments for achieving sound welds, an analytical method was developed that allowed to determine the optimum process parameters with a limited number of experiments. The predictions of the method were validated by LFW experiments, and sound samples without defects were produced. Microstructure evolution of the as-welded samples from the weld center to the base metal was investigated using laser confocal and field emission scanning electron microscopy (SEM) including electron back scatter diffraction (EBSD), energy dispersive spectrometer (EDS) and backscattered imaging (BSE). Post-weld heat treatment (PWHT), consisting of a γ' sub-solvus solutionizing followed by aging, was conducted on LFWed blocks. Then, microstructure evolution and mechanical testing were conducted on PWHTed samples and compared with the as welded blocks. The obtained results were correlated with microhardness as well as tensile testing at room temperature and 650 °C, and interpreted in terms of fundamental metallurgical processes. Macroscopic examination of the PWHTed joints revealed that the samples failed out of the weld zone, further demonstrating the appropriate selection of LFW processing parameters using the proposed analytical method. PWHTed samples exhibited better room and high temperature tensile properties compared to those of the as-welded samples. Microscopic examination of the fracture zones of the

* Corresponding author.

E-mail addresses: fmasoumi@yahoo.com (F. Masoumi), fatemeh.masoumi.1@ens.etsmtl.ca (F. Masoumi), mohammad.jahazi@etsmtl.ca (M. Jahazi).

samples showed that the higher levels of reprecipitation of γ' particles in the thermomechanically-affected zone (TMAZ) of the PWHT samples were associated to their higher tensile properties compared to the as welded ones.

© 2019 Published by Elsevier Ltd. This is an open access article under the CC BY-NC-ND license (<http://creativecommons.org/licenses/by-nc-nd/4.0/>).

1. Introduction

Linear friction welding (LFW) is a solid state joining technique for manufacturing of blades to integrated disks (blisks) or the repair of turbine disks in industrial gas turbines and jet engines. In addition, LFW allows a high degree of freedom in joint shape, making it superior to rotational friction welding which is limited to axisymmetric shapes. LFW has already been applied at the industrial scale to Ti alloys for compressor (i.e. low temperature) components [1–3] but its applications to high temperature components such as turbine blades, often made of Ni-based superalloys, is still facing many technological and scientific challenges [2,4,5].

LFW is fundamentally a hot deformation process. It is based on the reciprocal motion between a moving component and a stationary workpiece under compression loading. The process is composed of three main phases [6,7]: i) Conditioning phase, in which the parts are oscillated under specific frequency and amplitude, and are brought together under a small force for pre-determined time; ii) frictional phase, in which the compressive force is increased and heat is generated at the interface while one of the samples is oscillating, and oxide layers are removed in this phase; and iii) forge phase in which the amplitude is decreased to zero, and samples are brought together, and the weld is consolidated by the applied pressure.

Eight process parameters, namely: oscillation frequency, oscillation amplitude, applied friction force, axial shortening, ramp-up time, oscillation decay time, forging force and forging force time have found having important impacts on the strength and quality of linear friction welded components [1,5–7]. Among them, the oscillation frequency and amplitude along with the applied pressure are considered to be the main process inputs for most industrial LFW machines used by industry. Therefore, these variables should be optimized and adapted for each material as a function of its physical and mechanical properties [6]. Since the LFW process is very fast, the interface of the workpieces cannot be observed during welding and therefore indirect measurements or simulations have to be used for predicting temperature, deformation history and stress distribution in the weld joint. Additionally, LFW is a coupled thermo-mechanical process and this complexity is directly influencing the plastic flow of the materials and the metallurgical behavior of the joint during the welding process [8]. Due to the above complexities, many simplifications are used in both analytical and numerical models. For example, simple material models are used to account for strain hardening, strain rate hardening, and thermal softening effects [9] or often simple friction models are used to describe the contact interface [10]. The importance of reliable material flow stress behavior in performing these computations is vital; however, the available material property data in the literature is often limited to lower temperatures and strain rates [11]. For example, there are two opinions regarding the type of friction (sliding or sticking) at the weld interface when the material is plasticized [12]. The first one assumes a constant friction coefficient. While the second approach relies on a temperature dependent coefficient of friction in which changes in the welded interface conditions is taken into account by experimentally measured temperature. As reported by Maalekian [10], Buffa et al. [7] and Grujic et al. [13], change from sliding to sticking friction is a critical condition for forming solid state bond and therefore the determination of the transition point becomes very

important. However, it is difficult to find out the extent and contribution from each frictional mode and therefore, this interaction has been ignored in the analytical and numerical models especially when defects such as oxide layers are present at the interface. Although, it is expected that oxides are removed from the interface into the flash but they are also highly dependent on the material. For example, the chromium and aluminum oxides at the surface of Ni-based superalloys are thicker and more resistant than titanium oxides at the surface of a Ti-6Al-4V alloy [14,15]. Hence, in order to ensure their removal, the selection of the process parameters should be adapted to the material type. In addition, optimized LFW process parameters would also help reducing residual stresses generated during the welding process due to the plastic deformation and thermally induced strain by the workpieces [1,16–18]. Analytical and numerical approaches have both considered rigid or deformable bodies to obtain frictional heat at a specified stage [19,20]. One dimensional heat flow analysis has been used in the analytical methods to predict the outputs from the friction welding process [12,21,22]. 2D and 3D fully coupled thermomechanical finite element models based on explicit or implicit technique using ABAQUS, DEFORM, FORGE, ANSYS and ELFEN softwares have been developed to predict the evolution of temperature, strain rate, strain and stress within the welded parts [11]. However, some outputs, such as flash morphology, flash formation rate, interface contaminant expulsion, microstructure evolution and residual stress formation are difficult to obtain using analytical models [1,7]. In contrast, analytical models have faster calculation times and provide easier setups [12]. Despite their specific advantages, both analytical and numerical models fail to accurately estimate the input process parameters and therefore such parameters are initially assumed or values from the literatures are adopted [1,5–7,20] which inevitably introduce errors in the optimum selection of the process parameters. To date, most of the available studies on LFW are based on empirical and full factorial experimental plans that are time consuming and costly [23]. Therefore, it is important to develop new methods that would allow achieving optimum processing conditions with a minimum number of trials, particularly when it comes to expensive materials such as Ni-based superalloys with a high amount of refractory elements and complex processing stages.

Ni-based superalloys are the materials of choice for high temperature applications (above 800 °C) in gas turbines in aerospace and power generation industries [24]. Their high temperature strength is mainly due to the presence of second phase particles composed of the Ni_3Al intermetallic (of L1_2 structure), called γ' , or of Ni_3Nb intermetallic (of DO_{22} structure), called γ'' for alloys of the Inconel 718 class, and different types of carbides and nitrides [24–27]. During LFW of Ni-based superalloys, the material at the weld joint and its vicinity (Heat affected zone and thermomechanically affected zone) undergoes significant microstructural changes This includes dissolution of γ' precipitates and some of the carbonitrides, dynamic and post-dynamic recrystallization, bringing grain refinement, as a result of high temperature and deformation conditions [5,14,28]. In contrast, during cooling, reprecipitation of the second phase particles and possible grain growth take place. Residual stresses are usually produced in the heat affected zone because of the presence of misfit strains between the weld region and the base material. The refined grain size at the weld interface can reduce the residual stress while the fine γ'

Table 1Chemical composition and γ'/γ'' volume fraction of AD730™ compared to some other Ni-based superalloys (wt%) [46].

	Ni	Fe	Co	Cr	Mo	W	Al	Ti	Nb	B	C	Zr	V _f
718	Bal.	18	–	18	3	–	0.5	1	5.4	0.004	0.03	–	17
718Plus	Bal.	10	9	18	2.75	1	1.5	0.7	5.5	0.004	0.02	–	24
Waspaloy	Bal.	–	13.5	19.5	4.25	–	1.5	3	–	0.006	0.05	0.03	32
U720Li	Bal.	–	15	16	3	1.3	2.5	5	–	0.015	0.02	0.03	44
AD730™	Bal.	4	8.5	15.7	3.1	2.7	2.25	3.4	1.1	0.01	0.015	0.03	40

precipitates in this region are likely to strengthen the material and consequently, increase the level of residual stresses [16–18,29]. Furthermore, due to the deformation and temperature gradients the residual stresses are not uniformly and homogeneously distributed. All the above phenomena and the presence of residual stresses are expected to impact on mechanical and service properties of weld joint [30–35] and therefore they have to be reduced or eliminated through post weld heat treatment to avoid affecting the service properties. However, although extensive data is available on hot deformation of Ni-based superalloys [36–39], microstructure evolution during LFW and its impact on mechanical properties of welded Ni-based superalloys has been less investigated. Damodaram et al. [40] reported that reduction in average size and volume fraction of γ' precipitates results in decrease in mechanical properties of as-welded specimens [40]. Chamanfar et al. [41] and Daus et al. [42] observed a reduction in hardness value of the weld zone compared to base material, due to the dissolution of the strengthening precipitates, in LFWed Waspaloy and inertia friction welded IN718, respectively.

While some detailed work on microhardness, microstructure and residual stress analyses have been published on friction welded Ni-based superalloys [28,42–45], little data has been reported on the integrity of LFWed Ni-bases superalloys. Limited work published by Damodaram et al. [40] indicated that the best hardness and tensile properties of the welded material was obtained when the material was welded in solution treated condition, and subjected to direct aging after welding. Chamanfar et al. [41] also reported that below axial shortening of 2 mm LFWed Waspaloy showed weak integrity. Furthermore, most if not all the mechanical tests have been performed at room temperature, and therefore the results could not be directly applied to tensile properties at high temperatures which correspond to actual service conditions of these alloys.

The objectives of the present investigation are therefore twofold: i) develop a methodology for the determination of the optimum process parameters and fabricating sound LFW joints

using a minimum number of experiments; and ii) investigate and quantify the evolution of the microstructure, especially γ' precipitates and γ grain size, and its impact on hot tensile properties. The interactions between LFW process parameters and mechanical properties will be discussed and related to the mechanisms governing the evolution of the microstructure.

2. Experimental procedures

The material used for the LFW experiments is AD730™, a wrought Ni-based superalloy recently developed by Aubert & Duval, especially for the first stages of the turbine disks and seal rings with high mechanical properties of up to 750 °C [46]. Previous studies based on thermodynamic simulation [47–49] or phase extraction [50] have shown that the AD730™ alloy is characterized by a γ' volume fraction of about 40% in equilibrium condition at temperature below 500 °C. Considering that same alloy has been used in the present investigation, no γ' volume fraction measurement was conducted. AD730™ has mechanical properties close to Udimet 720Li and significantly higher than Inconel 718Plus, Waspaloy and Inconel 718. Table 1 shows a comparison between chemical composition and γ' volume fraction of these alloys [46]. Therefore, the microstructure evolution of AD730™ might not be similar to Waspaloy or Inconel 718, and the investigated alloy is expected to behave differently from these alloys.

Rectangular blocks $26 \times 13 \times 37$ mm³ (length \times width \times height) of the AD730™ alloy were WEDM (wire electrical discharge machining) extracted from a forged square bar provided by Aubert & Duval. The square bar had been subjected to solution treatment at 1080 °C for 4 h followed by air cooling. The composition of the alloy is given in Table 1. Differential Thermal Analysis (DTA) and Gleeble™ 3800 physical simulator were used to determine the dissolution temperatures of primary γ' at low (up to 2 °C/s) and high heating rates (up to 400 °C/s), respectively.

A method based on an analytical thermal analysis of the LFW

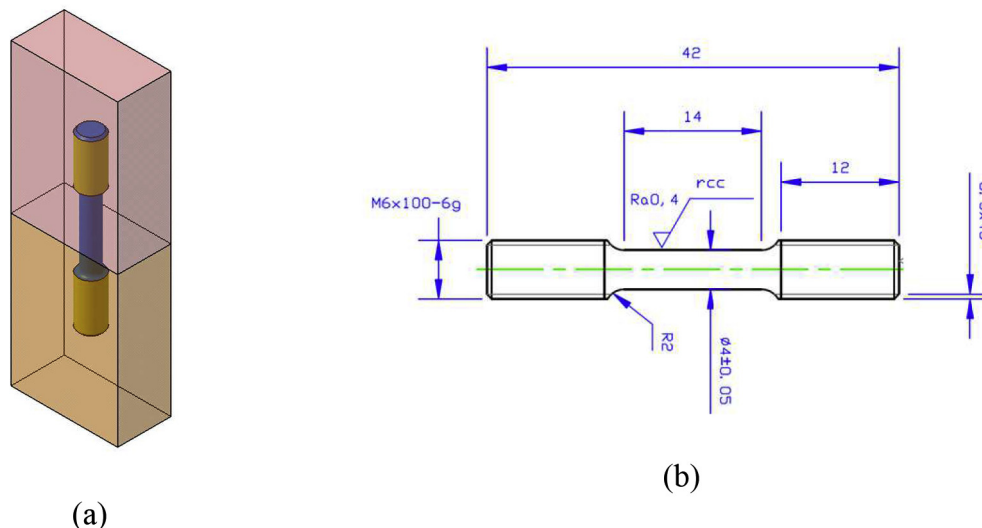


Fig. 1. Configuration of (a) tensile specimen inside LFWed sample and (b) specimen geometry for tensile tests according to ASTM A370 standard (all dimensions are in mm).

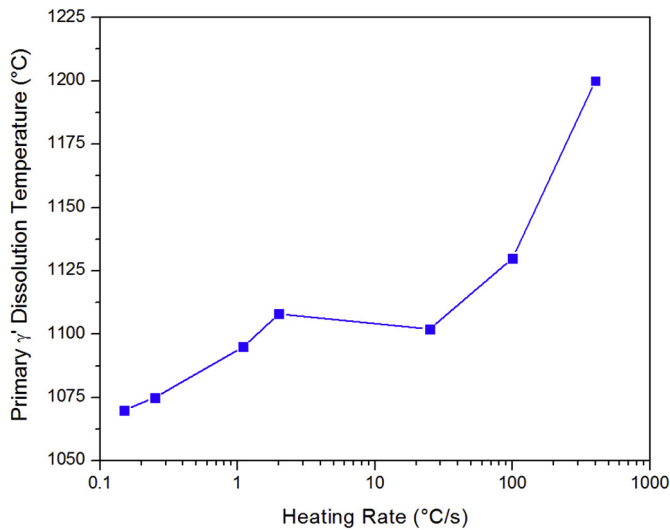


Fig. 2. Primary γ' dissolution temperature of the AD730™ at different heating rates. DTA and Gleeble™ 3800 physical simulator were used to determine the dissolution temperatures of primary γ' at low (up to 2 °C/s) and high heating rates (up to 400 °C/s), respectively.

process was developed to identify the critical process parameters and determine their optimum values in order to achieve sound welds with a minimum number of samples. The details of the proposed methodology will be provided in the next section.

Using the developed methodology only four trials were carried out and the optimum welding parameters for defect free joints were determined to be: friction pressure of 285 MPa, forge pressure of 580 MPa, frequency of oscillation of 40 Hz, and amplitude of 2.5 mm. The LFW experiments were carried out with an FW34-E20 LFW machine at TWI, Cambridge, UK.

Following the welding, one of the LFWed blocks was sectioned along the longitudinal axis into two pieces and the cross-sections were polished for microstructure analyses and microhardness measurements. Vickers microhardness profiles were obtained for LFWed samples with different heat inputs to evaluate weld strength. The tests were performed across the weld region using a load of 500 g and a dwell time of 15 s. Measurements were carried out from the weld interface to a distance of approximately 5 mm on either side of the interface within the parent material.

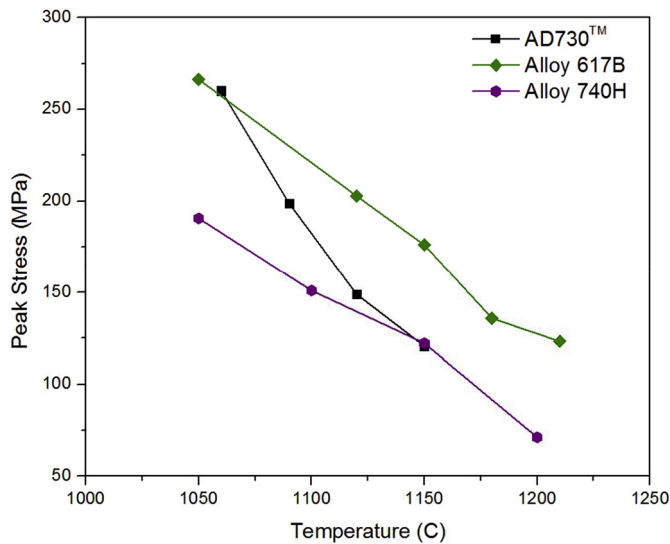


Fig. 3. Peak stress values of the AD730™ and the other nickel based superalloys at strain rate of 0.1 s⁻¹. Data on alloy 617B and 740H adapted from [38,60].

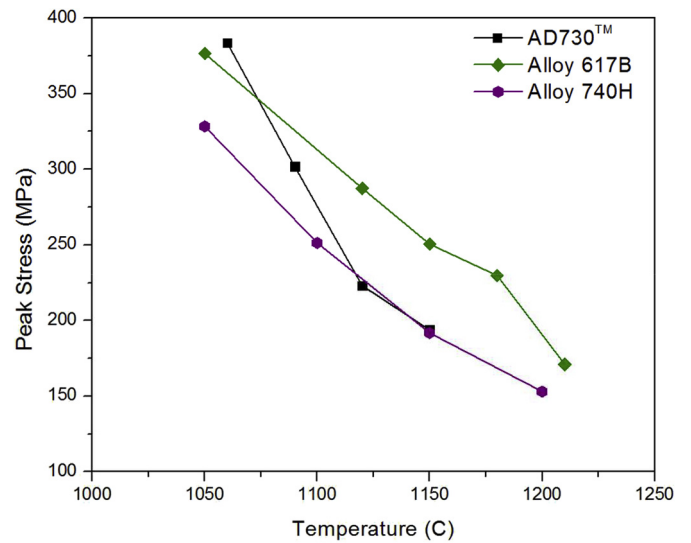


Fig. 4. Peak stress values of the AD730™ and the other nickel based superalloys at strain rate of 1 s⁻¹.

Tensile testing was conducted on as-LFWed and PWHTed samples. Therefore, some of the as-welded blocks were subjected to solution treatment and aging before tensile testing. Solutionizing was carried out in two steps: initially the samples were heated to 900 °C and held for 2 h. Then, they were heated at 0.15 °C/s to 1080 °C, held at this temperature for 4 h followed by air cooling. The aging treatment was conducted at 730 °C for 8 h followed by air cooling. The configuration of tensile test specimens inside LFWed sample and their geometry are reported in Fig. 1. The specimens were machined in such a way that the LFWed joint interface was located in the middle of the gauge length and perpendicular to the tension axis. Tensile tests were carried out at 20 °C and 650 °C using a constant strain rate of 10⁻³ s⁻¹ using an electromechanical “Instron8562” machine. Sample temperature was controlled using S-type thermocouples and the elongation in the gauge region was measured using a high temperature extensometer. During hot tensile tests, the temperature difference was controlled within ±1 °C using a controller.

Laser confocal microscopy (LEXTOS4100) and SEM (FEG-SEM Hitachi 8230) equipped with EDS, BSE and EBSD detectors were used for microstructure evolution analyses. Quantitative analyses

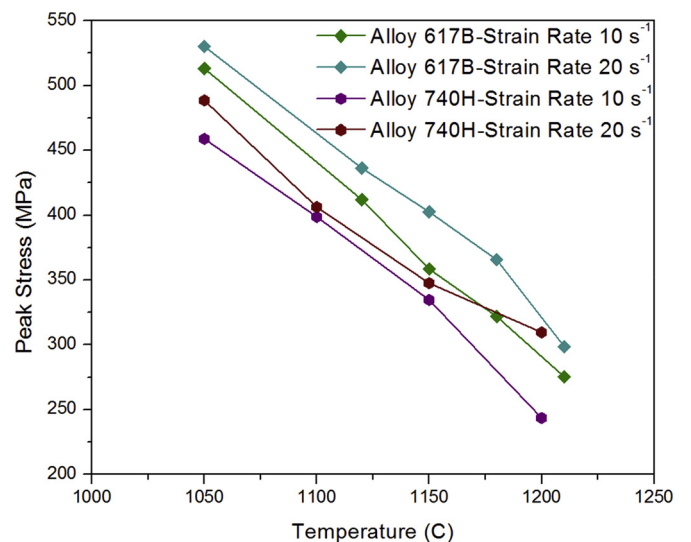


Fig. 5. Peak stress values of the various nickel based superalloys at strain rates 10 and 20 s⁻¹ [38,60].

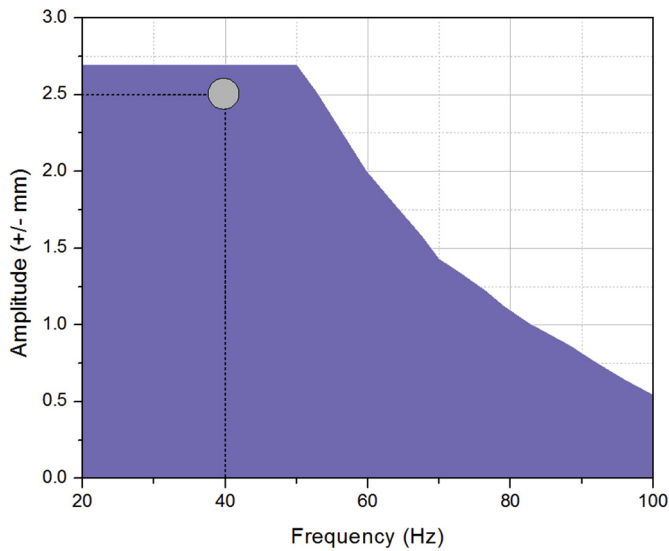


Fig. 6. Operating window for LFW machine (FW34 at TWI, Cambridge, UK).

of the size and volume fractions of the γ' precipitates were performed using digitized microscopic images and Image J analysis software. Each reported value for γ' volume fraction is an average of 5 measurements. In each case, area measurements on more than 100 precipitates were carried out. The particle radius was then calculated as the radius of a circle whose surface area equaled that of the corresponding particle.

3. Determination of optimum LFW process parameters

3.1. Selection of friction and forge pressures

The friction and forging phases in LFW can be considered as an upsetting process, consisting in deforming a metal between two flat dies. In this case, a plane-strain hot compression with sticking friction condition could be used to analyze these two stages. Using the slab analysis method for plane strain compression, the applied average pressure can be estimated according to Eq. (1) [51–53]:

$$P_{ave.} = 2k \left(1 + \frac{\mu a}{h} \right) \quad (1)$$

where k is the shear strength, μ is the constant coefficient of friction, a and h are width and height of the specimen, respectively.

By considering plane strain compression, k can be expressed as:

$$k = \frac{\bar{\sigma}}{\sqrt{3}} \quad (2)$$

where $\bar{\sigma}$ is the flow stress.

By substituting k into Eq. (1), the minimum pressure for the onset of plastic flow during LFW process will become:

$$P_{ave.} \geq \frac{2\bar{\sigma}}{\sqrt{3}} \quad (3)$$

Table 2

Linear friction welding parameters determined and used for AD730™ Ni-based superalloy.

Test condition	Oscillation amplitude (mm)	Oscillation frequency (Hz)	Friction pressure (MPa)	Forging pressure (MPa)	Heat input (W/m ²)
^a W1	2.5	40	133	330	3.192×10^7
W2			150	265	3.600×10^7
W3			187.5	265	4.500×10^7
W4			285	580	6.840×10^7

^a W: weld.

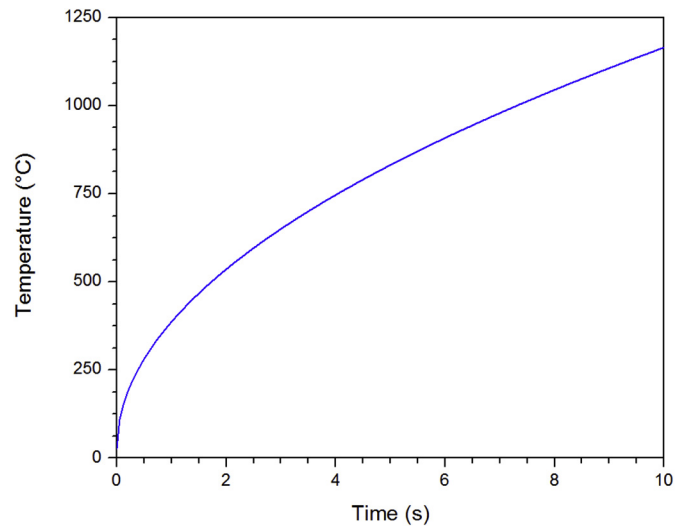


Fig. 7. Temperature variation with time for different LFW process parameters for the W1.

Therefore, accurate estimation of material flow stress is a necessary condition to determine the minimum pressure for plasticizing the material. In its most general form, the flow behavior of a material is a function of strain (ϵ), strain rate ($\dot{\epsilon}$) and temperature (T) [11,54,55]. In the present investigation, a combination of published data on hot deformation and LFW of Ni-based superalloys and analytical calculations were used to estimate the flow stress and its relation as a function of the above variables:

3.1.1. Strain during LFW

It is well known that due to the dynamic nature of the LFW process, the exact determination of strain at the interface during LFW using experimental method is very difficult. Using 2D or 3D finite element simulation, the equivalent plastic strain fields have been predicted [56–59]. The equivalent plastic strain distributions using 2D FEM simulation were estimated by Yang et al. [56] during friction welding process of a typical Nickel-Based superalloy. Based on the authors' results, the plastic strain at the center of the weld interface reached about 12. However, the strains at 1 mm and 8 mm far from the weld line were much smaller and estimated to be approximately 0.8 and 0.01, respectively. In addition, by 3D coupled thermo-mechanical simulation, two different maximum strain values of 2.7 and 3.6 at the interface region were attained [57,58]. The previous works were based only on simulation with no experimental support, other authors [59], according to thermo-physical experimental work which it simulates LFW, have reported strain values in the range 0.1 to a maximum of 0.8. Analysis of the published data indicated that, the flow stress curves of the Ni-based superalloy deformed in the strain rate range of 0.01 s^{-1} to 20 s^{-1} and in the temperature range of $940 \text{ }^\circ\text{C}$ – $1200 \text{ }^\circ\text{C}$, showed the occurrence of peak stress followed by a steady state flow behavior [38,59–64]. Furthermore, the strain corresponding to the peak flow stress was between 0.1 and 0.2 and the flow stress became steady around 0.7. A comparison of mechanical and metallurgical behavior between the Ni-Based superalloys in the literature and the

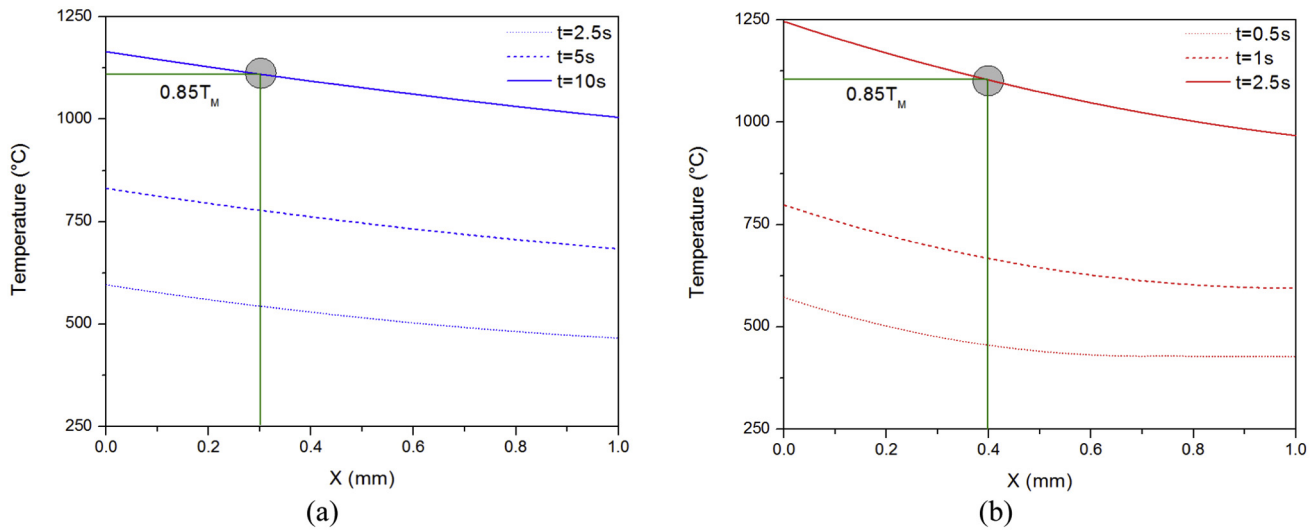


Fig. 8. Temperature distribution with various times along the x-axis with (a) the lowest and (b) the highest heat input.

AD730™ used in the present investigation showed that they are quite similar. Thus, in this research, the peak, 0.1 and steady state stress, 0.8 (upper and lower stress levels with the remaining stress values being between these two ranges), were used.

3.1.2. Strain rate during LFW

A wide range of strain rate values (between 0.1 and 2000 s^{-1}) has been proposed for LFW [5–7]. However, the majority of the authors have reported strain rates between 0.1 s^{-1} and 20 s^{-1} . The case of 2000 s^{-1} has been based only on simulation results with no experimental support [65]. Vairis et al. [66] reported that strain rate has the minimum value at the friction stage of LFW and reaches the highest value during the forge phase. Thus, in the present work, the friction pressure was estimated at a strain rate of about 0.1 s^{-1} while the forge pressure was calculated based on the available data on high strain rate values of 20 s^{-1} .

3.1.3. Deformation temperature estimation

Temperature should be high enough to allow easy plasticization of the metal at the weld interface during LFW. However, it should not be too high in order to prevent the formation of excessive flash or local melting at the grain boundaries [67]. Considering that the strength of the Ni-based superalloys is strongly dependent on the presence of γ' particles, the selection of the LFW process parameters must be optimized to attain a high enough temperature so that maximum dissolution of γ' particles is reached at the weld interface. Li et al. [6] also reported that the weld interface temperature during LFW of the Ni-based superalloys was between 0.75 and 0.95 of the melting temperature (T_M). Temperature measurements using an infrared thermal imaging instrument indicated that the temperature at the joint interface was about 1100 °C (i.e. 0.82 of the melting temperature) during friction stage of LFW of GH4169 Ni-based superalloy [56].

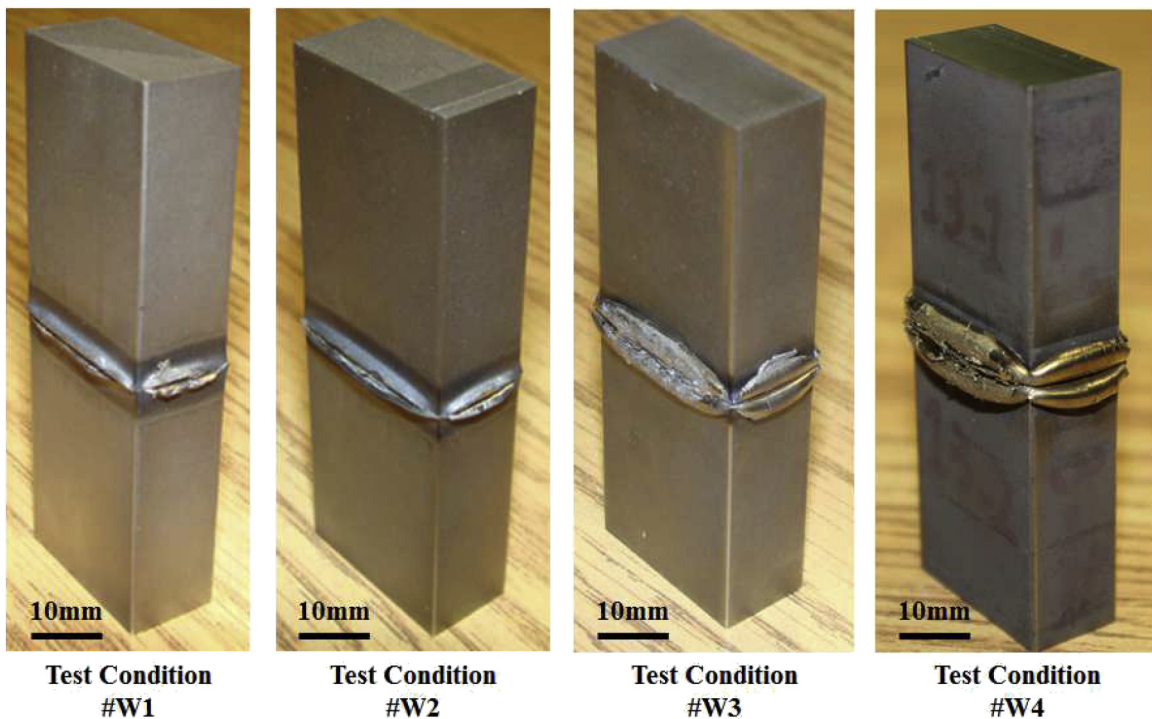


Fig. 9. Photographs of side views of the LFWed AD730™ joints. Minimum flash is observed in the test condition W1 while test conditions W3 and W4 present well-formed flash.

It must be noted that as the dissolution temperature of the primary γ' particles varies with the heating rate [14,30] and since the heating rate varies at different locations from the joint interface, the dissolution kinetics of the γ' particles is expected to change with the distance from the weld interface and must be taken into consideration.

The influence of heating rate on primary γ' dissolution temperature for the AD730™ alloy is shown in Fig. 2. It can be seen that the lowest temperature for γ' dissolution is around 1060 °C. Thus, the minimum temperature that needs to be reached before the application of deformation in the initial stage of the LFW process was considered to be 1060 °C. On the other hand, considering that the melting temperature of the investigated alloy is about 1350 °C [46], the maximum acceptable temperature at the weld interface was estimated to be 1150 °C (0.85 T_M).

3.1.3.1. Estimation of the friction pressure. The peak stress values for AD730™ and some other Ni-based superalloys [38,60] which are similar to AD730™ in the temperature range of 1000–1250 °C and for strain rates of 0.1 s⁻¹ and 1 s⁻¹ are shown in Figs. 3 and 4. In these curves, only the one for AD730™ was adjusted for the friction pressure calculation. Based on the above analysis, to estimate friction pressure, the peak stress at strain rate of 0.1 s⁻¹ and

deformation temperature of 1060 °C to 1150 °C were used to calculate the friction pressure. From Fig. 3, it can be found that the corresponding peak stress at about 1060 °C is 260 MPa while it is around 120 MPa at 1150 °C. Then, according to Eq. (3), friction pressure for AD730™ was calculated to be ranging from 133 to 285 MPa.

3.1.3.2. Influence of adiabatic heating. For accurate calculation of the forge pressure, temperature increase due to deformation heating needs to be considered. Since adiabatic heating is only present during the friction stage, it was only estimated for a strain rate of 0.1 s⁻¹ (corresponding to the friction phase of LFW) and 1 s⁻¹ (corresponding to the end of friction phase of the LFW process). The effect of adiabatic heating can be estimated by $\Delta T = \frac{0.95\eta}{\rho C_p} \int_0^\epsilon \sigma d\epsilon$ [51]. In this equation, η is the thermal efficiency (63.5% for strain rate of 0.1 s⁻¹ and 95% for strain rate of 1 s⁻¹), ρ the density of the alloy (8155.33 kg·m⁻³ at 1150 °C), C_p the specific heat (792.68 J·kg⁻¹·K⁻¹ at 1150 °C), ϵ the maximum strain (0.8) and σ maximum flow stress (peak stress) during hot deformation. The values of the physical properties were calculated for AD730™ using Thermo-Calc® with the TCNI5 database.

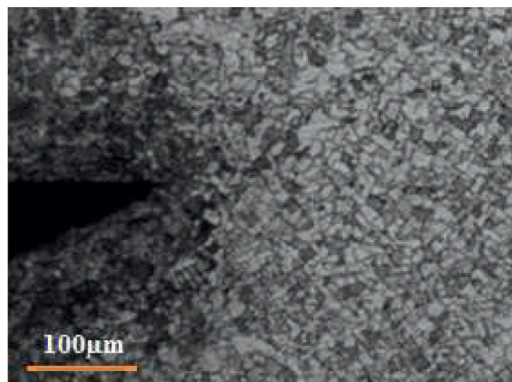
In the curves shown in Figs. 3 and 4, only the one for AD730™ was adjusted for adiabatic heating calculation. From these figures,



(a)



(b)



(c)

Fig. 10. Macrograph of W1 and W4: (a) Wavy interface with presence of oxides of W1 (b) smooth interface of W4 (c) higher magnification of the red box showing no voids or oxides.

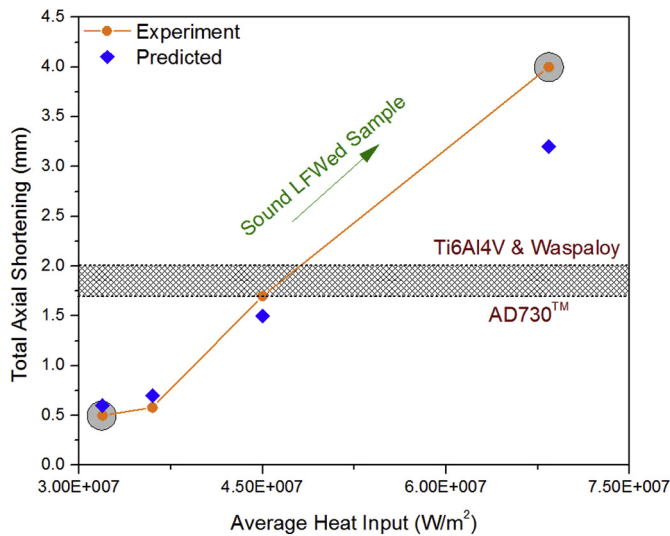


Fig. 11. Variation of axial shortening with the expected heat input.

the ‘adjusted’ peak stress at 1150 °C is approximately 120 MPa at strain rate of 0.1 s⁻¹ while it is around 290 MPa at strain rate of 1 s⁻¹. Using the above data, Δ*T* was calculated to be ~10 °C for a strain rate of 0.1 s⁻¹ and ~30 °C for a strain rate of 1 s⁻¹. Therefore, the maximum weld interface temperature or the upper limit of deformation temperature at the end of friction stage for a strain rate of 1 s⁻¹ was estimated to be approximately 1200 °C.

3.1.3.3. Estimation of the forge pressure. In order to estimate the average forge pressure, as presented in Eq. (3), the temperature dependence of the peak stress at high strain rates is needed. However, such data is not available for AD730™, and the only available data on highest strain rate values (10 and 20 s⁻¹) is for 617B and 740H Ni-based superalloys [38,60]. In order to evaluate the possible use of the data for the two above alloys for AD730™, a comparison between the peak stress behavior at lower strain rates (0.1 and 1 s⁻¹), AD730™ has a similar behavior to 617B and 740H superalloys. Furthermore, as reported in [38,60], in both alloys, γ’ precipitates are dissolved in the 1060 °C–1150 °C temperature

interval which is very similar to AD730™ alloy. Therefore, the measured peak stress for these alloys were used for the calculations of forge pressure at strain rates of strain rates of 10 and 20 s⁻¹ as shown in Fig. 5.

From Fig. 5, it can be seen that the peak stress for the weld joint temperatures of 1060 °C and 1200 °C varies between 530 MPa and 240 MPa, respectively. Using the flow stress at strain rate of 20 s⁻¹ in the 1060 °C–1200 °C interval and using Eq. (3), the forge pressures during the LFW process of AD730™ alloy were calculated to be between 265 MPa and 580 MPa.

3.2. Estimation of oscillation frequency and amplitude

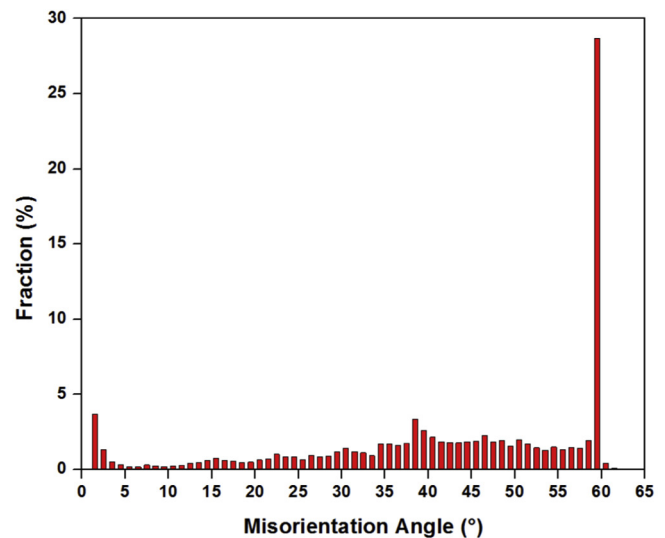
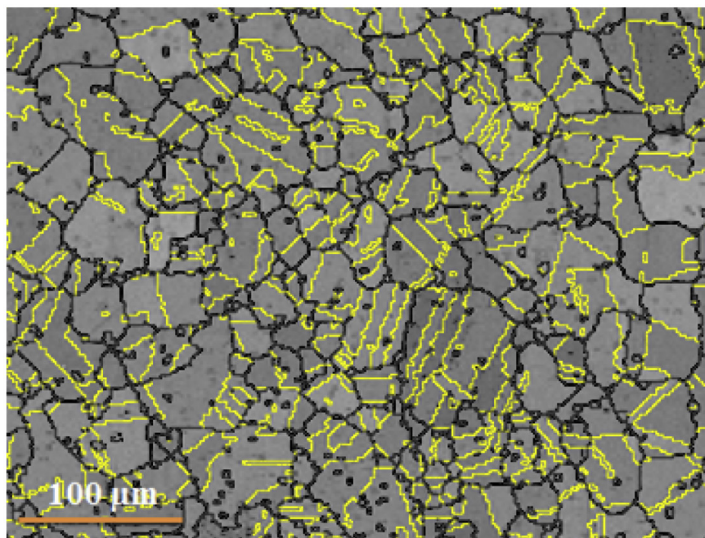
The oscillation frequency and amplitude also influence the maximum weld line temperature. By increasing these two parameters, the weld interface temperature increases rapidly at the early stages of the LFW process and then reaches an almost stable state. In order to quantify the impact of these two parameters, Addison’s equation [68] was used:

$$v_r = 4\alpha f \tag{4}$$

where *v_r* is the rubbing velocity, α and *f* are the oscillation amplitude and frequency.

A sound LFW joint can be formed by increasing the rubbing velocity which may increase the heat input, and consequently, higher temperature and removal rate of oxide layers are produced. Therefore, the rubbing velocity has to be kept as a maximum value in the optimization process. The maximum values were selected for oscillation amplitude and frequency within the operating window of the LFW machine. Fig. 6 illustrates the recommended amplitude and frequency parameters for the LFW machine at TWI, Cambridge, UK, used in this study. As shown in Fig. 6, the highest oscillation amplitude was about 2.7 mm, and the highest allowable amplitude was 2.5 mm which was selected for the welding trials. Similarly, the highest allowable oscillation frequency was 40 Hz, which was used for the tests. On this basis, the maximum rubbing velocity from Eq. (4) was calculated to be 400 mm·s⁻¹.

According to the above analysis, using analytical calculation, machine capability, and data in the literature, and with the view to reaching a defect free joint with optimum mechanical properties, an experimental plan was designed using the welding conditions



(a) (b)

Fig. 12. (a) EBSD map of the base material and the yellow lines are twin boundaries, (b) misorientation distribution in the parent material.

Table 3

Distribution of grain orientations from the base material to the weld region of W4.

Microstructural region (mm)	HAB % (between 15 and 55 misorientation)	LAB %	Twin %
Base material	57	9	34
1.8–2	43	27	30
0.8–1	17	61	21
0.6–0.8	20	65	15
0.4–0.6	27	60	12
0–0.4	40	56.1	3.9

provided in Table 2. Among the four variables of the LFW process, i.e. oscillation frequency, amplitude, friction and forge pressure, the first three provide heat at the interface while the fourth one controls the joint integrity. As discussed, the highest allowable values were considered for oscillation frequency and amplitude in the four trials. Then, trials 1 and 4 were conducted at the lowest and highest limits of calculated friction and forge pressures, respectively. For trials W2 and W3, intermediate values of friction and forge pressures were selected between the minimum and maximum values.

3.3. Estimating the heat input

In order to estimate the heat input in the friction phase for the selected LFW process parameters reported in Table 2, the following equation was used by several authors [1,6,10,69]:

$$HI = \mu v_r P_{Fric}. \quad (5)$$

where μ is the friction coefficient, v_r and P_{Fric} are the rubbing velocity and friction pressure. For the calculation purposes, a fixed rubbing velocity of $400 \text{ mm} \cdot \text{s}^{-1}$ was considered and the friction coefficient was taken equal to 0.6, as reported in the literature [9,10,56]. As presented in Table 2, the higher friction pressure will generate more heat at the weld interface which will lead to higher deformation rate and hence higher axial shortening, if the appropriate forging pressure is applied. Based on Eq. (5), W1 and W4 have the lowest and the highest heat input, respectively.

3.4. LFW process time

To determine the optimum linear friction welding time, an analytical procedure based on a one dimensional (1D) thermal analysis was employed. During the LFW process, heat losses by radiation and convection are usually negligible [10]. Therefore, as also reported by several authors [70–73], the temperature distribution in each solid part can be determined by solving the 1D heat conduction equation. Heat equation for three-dimensional without energy generation is given by:

$$\frac{\partial T}{\partial t} = a \left(\frac{\partial^2 T}{\partial x^2} + \frac{\partial^2 T}{\partial y^2} + \frac{\partial^2 T}{\partial z^2} \right) \quad (6)$$

where T is the temperature, t is the time, x , y , z are the heat flow directions, and a is the thermal diffusivity. The thermal diffusivity is related to thermal conductivity λ , density ρ and specific heat C_p through the following equation [71]:

$$a = \frac{\lambda}{\rho C_p} \quad (7)$$

The analytical solution for the 1D transient temperature distribution with time is given by [73]:

$$T(x, t) = T_i + \frac{\dot{q}}{2\lambda} \left[\sqrt{\frac{4at}{\pi}} \exp\left(-\frac{x^2}{4at}\right) - x \operatorname{erfc}\left(\frac{x}{2\sqrt{at}}\right) \right] \quad (8)$$

In the above equation, \dot{q} (W/m^2) is the rate of heat generation and T_i is the ambient temperature. It should be noted that it is assumed that the generated heat diffuses along the x direction. According to Eq. (8) for $x = 0$, the temperature distribution is given by:

$$T(0, t) = T_i + \frac{\dot{q}}{\lambda} \sqrt{\frac{at}{\pi}} \quad (9)$$

Using Eq. (8) and the analysis made in Section 3.1.3, the maximum temperature of the weld interface was estimated to be about 1250°C at the end of the process. In the calculations, the thermal diffusivity and thermal conductivity of the investigated alloy were taken equal to $11.15 \text{ W} \cdot \text{m}^{-1} \cdot \text{K}^{-1}$ and $2.79 \times 10^{-6} \text{ m}^2 \cdot \text{s}^{-1}$, respectively as reported in [46].

Using the LFW process parameters given in Table 2, Eqs. (5) and (9), the temperature profiles were calculated and are presented in Fig. 7. The W1 has minimum heat input with the interface reaching approximately the estimated maximum weld line temperature after about 10 s. In contrast, for the W4, in which frictional heat input is the highest, the estimated maximum weld line temperature is obtained after 2.5 s. In order to insure better weld integrity, a constant processing time of 10 s was used in the experiments. The selected processing time is therefore expected to be sufficient for inducing plastic deformation over the entire weld interface.

3.5. Estimating the axial shortening

Based on Eq. (5), W1 and W4 have the lowest and the highest heat inputs, respectively. Then, temperature distribution in the stationary part for these two test conditions was calculated according to Eq. (8), and the results are shown in Fig. 8(a, b). The evolution of temperature with position from the weld interface and heating period times can be clearly observed in these figures. For both conditions, the temperature in the bulk of the material increases with increasing welding process time. It is a reasonable approximation to assume that when the material flow starts at $0.85T_M$, a significant volume fraction of the secondary and primary γ' precipitates have already been dissolved. Therefore, locations at 0.3 mm and 0.4 mm away from the weld interface are expected to be easily deformed under W1 and W4, respectively. As shown in Fig. 8(a), with the minimum heat input, 0.6 mm plastic deformation is produced in 10 s, while with the maximum heat input, an overall deformation of 0.8 mm is produced after 2.5 s (i.e. 3.2 mm after 10 s) (Fig. 8(b)). Hence, the corresponding axial shortening values predicted from the temperature profiles are around 0.6 mm and 3.2 mm for low and high heating inputs, respectively. In the next

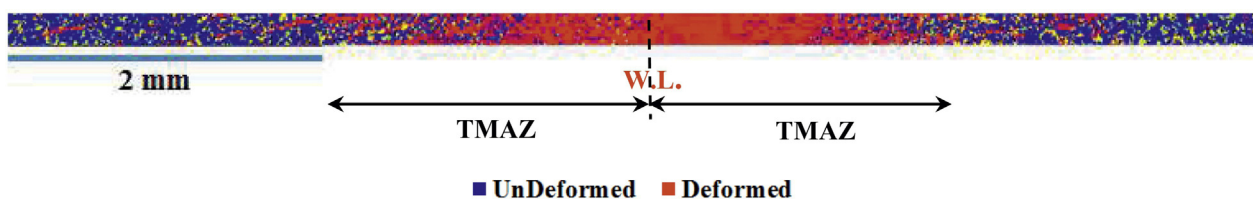


Fig. 13. Low magnification EBSD map of the transversal cross section of the LFWed W4. Red zones depict deformed areas and blue areas are undeformed zones.

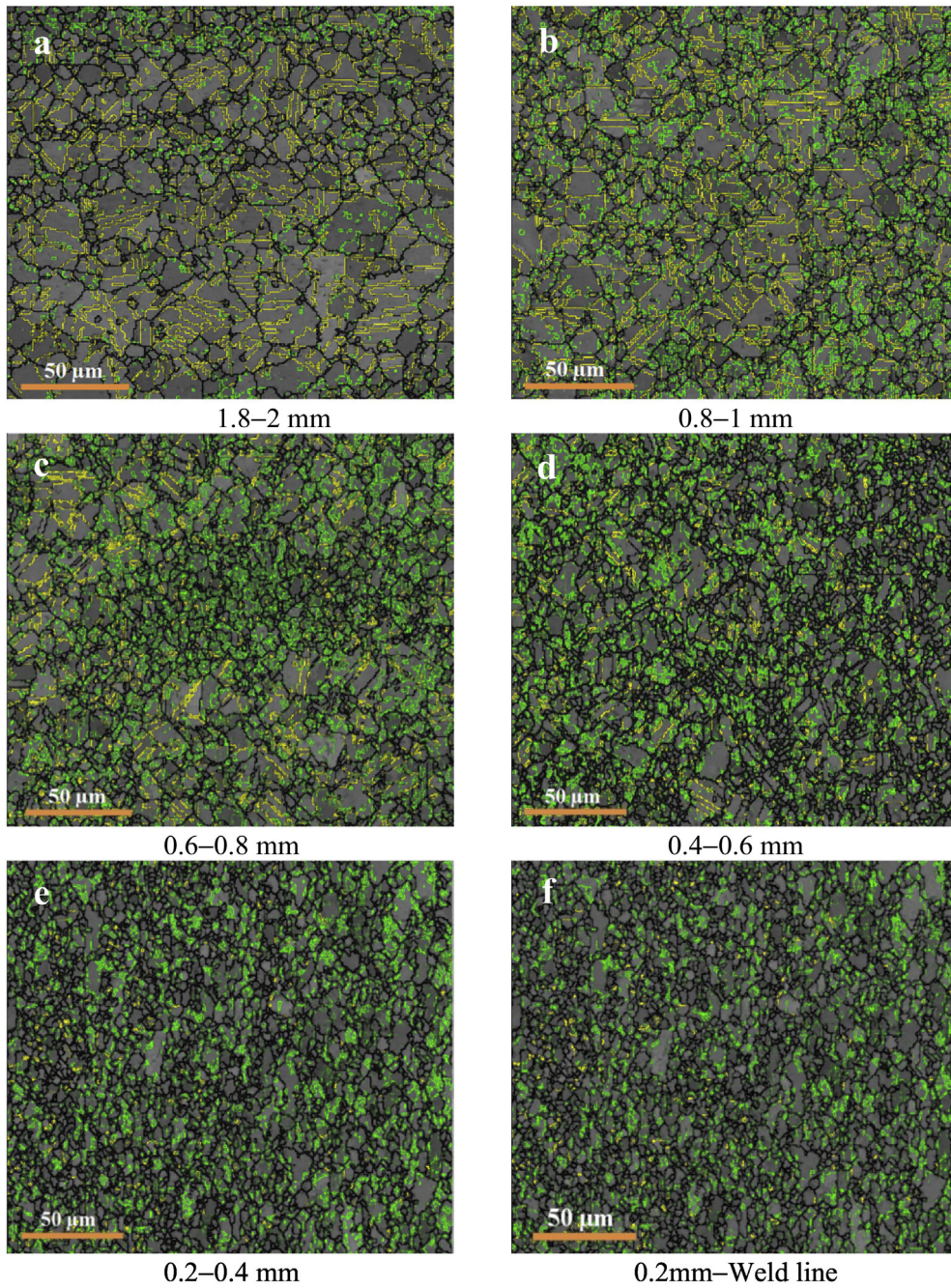


Fig. 14. EBSD grain boundary maps showing microstructural changes of the LFWed W4. (a) 1.8–2 mm, (b) 0.8–1 mm, (c) 0.6–0.8 mm, (d) 0.4–0.6 mm, (e) 0.2–0.4 mm from the weld interface and (f) 0.2 mm to weld line. In the maps, LABs, HABs and twin boundaries are depicted as green, black and yellow lines, respectively.

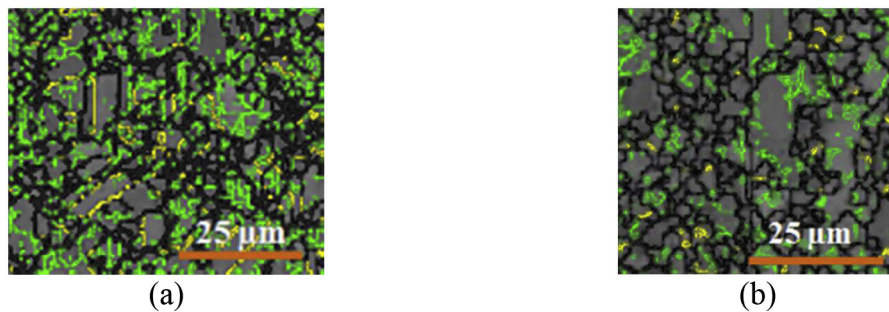


Fig. 15. EBSD grain boundary map of the LFWed W4; (a) 0.6 mm and (b) 0.2 mm from the weld interface showing grain boundary bulging.

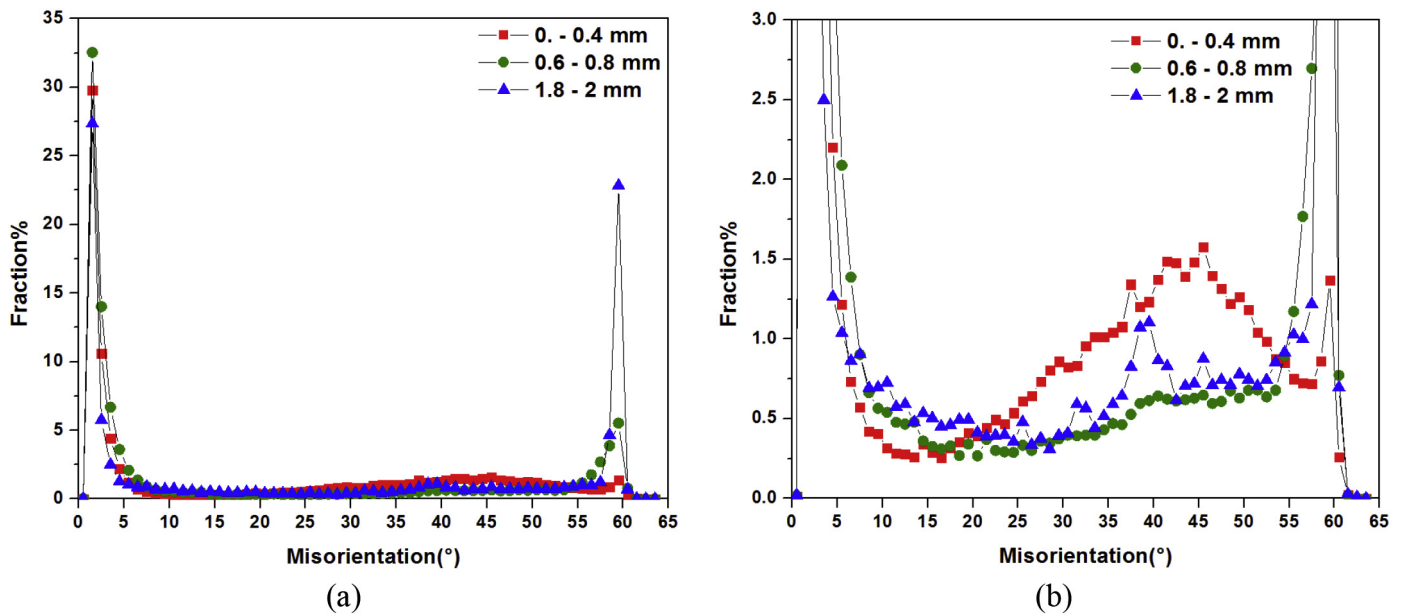


Fig. 16. (a) Misorientation distribution in weld zone(0–0.4 mm), TMAZ(0.6–0.8 mm) and base metal (1.8–2 mm) of the LFWed W4. (b) Higher magnification of (a).

section, the metallography (macro and micro) examination of the samples for 4 testing conditions will be presented and the obtained results will be compared and validated with the above predictions.

4. Macrostructure

4.1. Macroscopic evaluation of the joint after LFW

Fig. 9 shows the LFWed samples for the four selected conditions. It can be seen that while a very little flash is formed under conditions 1 and 2, a well-formed flash, and consequently better joint integrity, is produced with W3 and W4. The measured axial shortenings were 0.5 mm, 0.58 mm, 1.7 mm and 4 mm for W1 to W4, respectively.

The macroscopic features of the LFWed W1 and W4, which have respectively the minimum and maximum flash, are compared in Fig. 10(a, b). Impurities like oxide layers appeared in a wavy form at the weld interface of W1 while under test condition W4 a defect-free joint was produced. Similar observations have also been reported on other LFWed joints, and related to the reciprocating motion of the parts during the LFW process [74]. Visual inspection of the weld interfaces showed that bifurcated flash was formed during LFW. In W4, the flash was connected around the corners of the specimen which is indicative of its high integrity while that was not the case for W1. Further examination of W4 weld line at higher magnifications (Fig. 10(c)) did not reveal oxide particles, voids or microcracks at the corner of the LFWed sample, indicating that all the oxides were removed from the weld line due to sufficient extrusion of the interface material. Thus, further macroscopic and microscopic evaluations as well as evaluation of mechanical properties were performed on W4.

Fig. 11 shows the heat input calculated based on Eq. (5) versus the measured and the predicted axial shortening (calculated based on Eq. (8)) for the four test conditions. The predicted axial shortenings were 0.6 mm, 0.7 mm, 1.5 mm and 3.2 mm for W1 to W4, respectively. The absolute difference between the predicted and experimentally measured axial shortening is maximum 0.2 mm for heat inputs lower than 4.5×10^7 (W/m^2) (W3) while it is 0.8 mm for the highest heat input (W4). By comparing the analytical results to the experimental ones, it can be seen that up to a heat input value of 3.6×10^7 (W/m^2) the predicted axial shortening is slightly higher

than the measured one while it is always lower than the experimental value by the increase in the heat input. This means that material extrusion during LFW process is strongly correlated with the heat input. Thus, using Fig. 11, a threshold for remarkable flash formation could be defined as a function of the selected LFW parameters (i.e. heat input). This threshold is limited to a 1.7 or 2 mm axial shortening (gray zone) for the Nickel based superalloys and titanium alloys. It must be noted that, although the difference between the predicted and measured axial shortening is reasonable, the observed difference could be due to the use of a one dimensional analytical model. A better conformance is expected, if 2D or 3D numerical simulations are developed in future.

No oxide particles were observed at the weld interface of AD730™ with axial shortening larger than 1.7 mm. Therefore, in order to obtain a sound LFW joint for AD730™, a minimum axial shortening of 1.7 mm is necessary. This finding is in agreement with those reported by [15,41] who observed defect free joints with adequate room temperature tensile properties with axial shortenings of more than 2 mm on LFW of Ti6Al4V and Waspaloy. Furthermore, the obtained experimental results confirm the validity and reliability of the proposed analytical approach in identifying LFW process parameters with a minimum number of welding experiments.

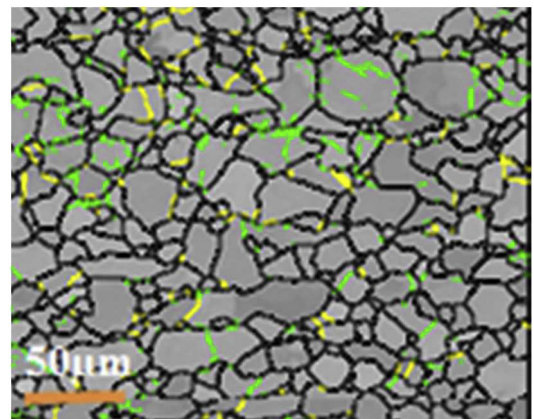
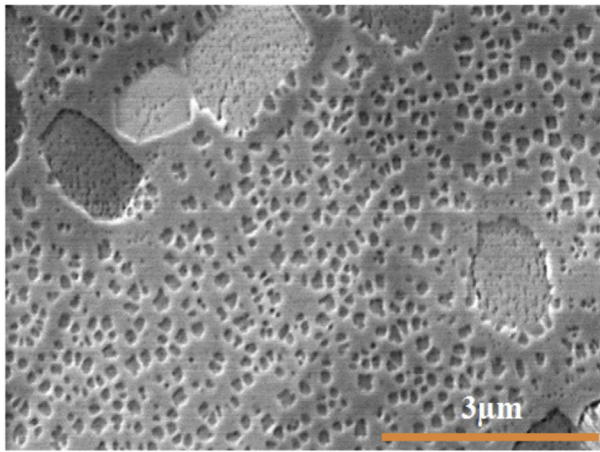
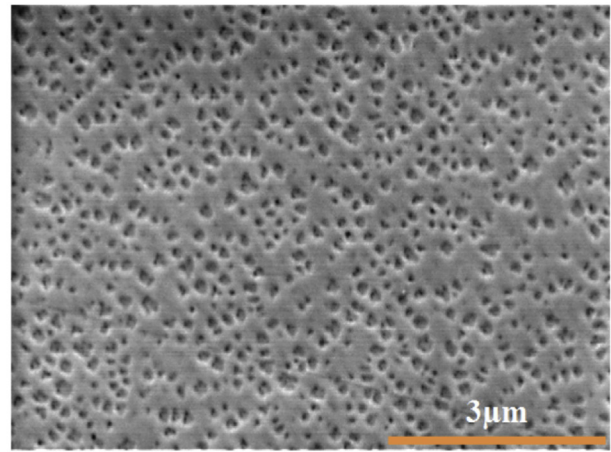


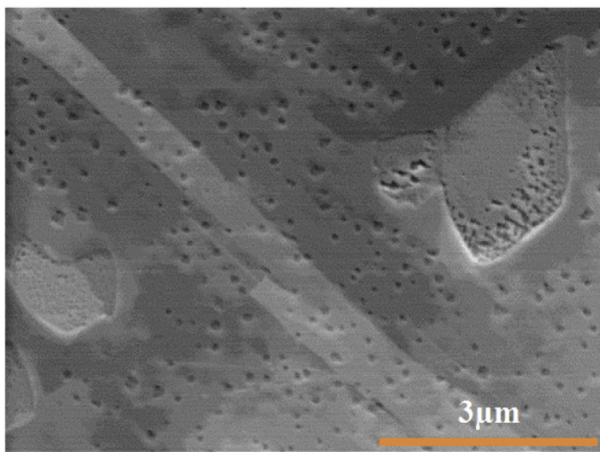
Fig. 17. EBSD grain boundary map of the LFWed W1 at the weld interface.



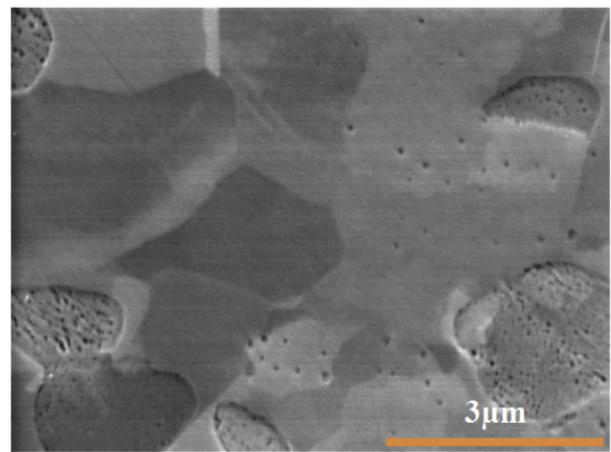
(a) Base metal



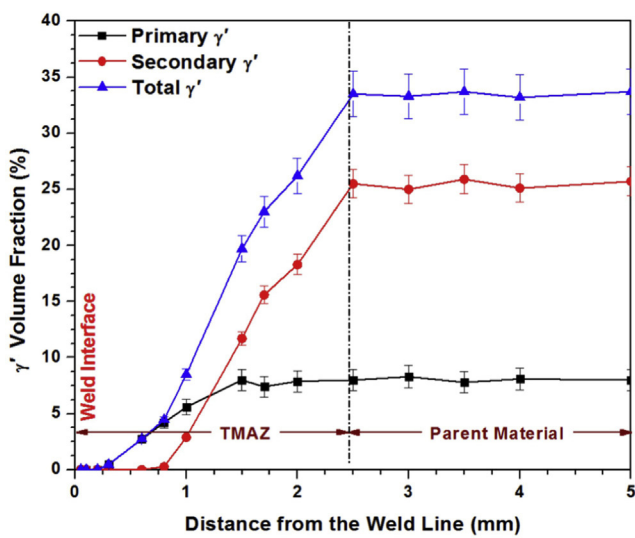
(b) 1.7 mm from the weld interface



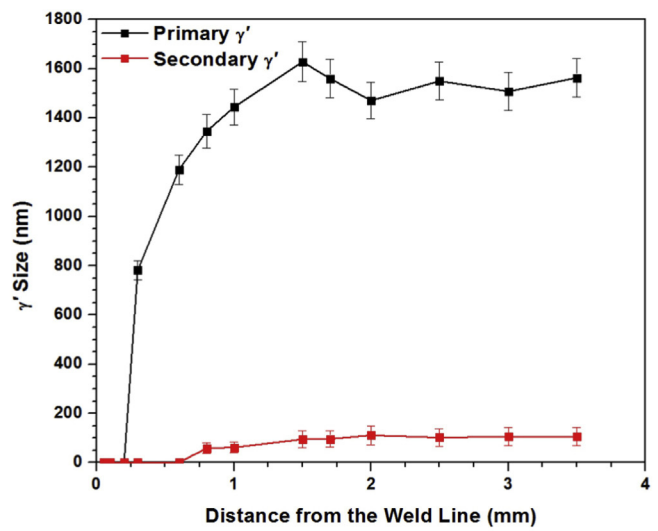
(c) 1 mm from the weld interface



(d) 0.8 mm from the weld interface



(e)



(f)

Fig. 18. FEG-SEM images of γ' precipitates in W4 (a) in the parent material, (b) to (d) respectively at 1.7, 1, and 0.8 mm from the weld interface. (e) Variation of γ' volume fraction as a function of the distance from the weld interface. (f) Average γ' size at various positions from the weld line. The standard deviations of the γ' volume fraction and size measurements are shown by error bars.

5. Microstructure

5.1. Grain size evolution at the weld Interface

The EBSD map of the base material is provided in Fig. 12(a) and the distribution of grain misorientations in Fig. 12(b). An average grain size of approximately $40\ \mu\text{m}$ was calculated based on ASTM E112 standard and Image J analysis software. About 57% of the grain boundaries were high angle in character (HAB) with misorientations ranging from 15 to 55° . Low angle grain boundaries (LABs defined in the misorientations range of 1 to 15°) fraction was as low as 9% with most of them clustered within some grains as shown by black dots in Fig. 12(a). Finally, about 34% of the microstructure was composed of $\Sigma 3$ twin boundaries (Fig. 12(b)). Table 3 summarizes the distribution of grain orientations in the base metal and its evolution from the base metal to the weld interface.

Fig. 13 shows an EBSD map of W4 over a large distance covering both sides of the weld line. Since the measured distance was very large, the width of the recording window was small; however, this does not affect the interpretation of the obtained results. In Fig. 13, the area with concentrated red zones, with a width of approximately 4 mm corresponds to the TMAZ, and shows a heavily deformed region where the misorientation changed significantly during LFW process.

In Fig. 14, the evolution of the microstructure at different locations from the weld line is presented. The LABs, HABs and $\Sigma 3$ twin boundaries (within 5° tolerance) are depicted as green, black and yellow lines, respectively. At approximately 2 mm far from the weld line, LABs start to develop within parent grains or near parent grain boundaries (Fig. 14(a)). Therefore, this zone could be considered as the outer edge of the TMAZ. The LABs have very low misorientations, and the HAB fraction in this region is close to that of the base material. Furthermore, twin boundaries are transformed into random boundaries and their fraction is reduced from 34% to 30% and gradually disappeared from the microstructure (Fig. 14(b)–(f) and Table 3). This phenomenon is attributed to strain-induced crystallographic rotations of the twins and their surrounding matrix from their initial orientations [75].

Closer to the weld zone, LABs are observed within most of the original grains, and mostly concentrated close to the original grain

boundaries. As shown in Table 3, the LABs fraction significantly increased from 9% in the base material to 60% at 0.6 mm from the weld line while the twin fraction substantially reduced from 34% in the base material to 12%. Grain boundary bulging was clearly visible in the microstructure located at 0.4–0.6 mm from the weld line, as shown in Figs. 14 and 15. Some of these serrated boundaries transform into fine grains indicating the occurrence of dynamic recrystallization (DRX) [76]. This process probably starts from $L = 0.8$ mm, as HAB fraction in the misorientation range of 15 – 55° gradually increases from 17% at $L = 1$ mm to 20% at $L = 0.8$ mm (Table 3 and Fig. 14). The average grain size at $L = 1$ mm zone was determined to be about $25\ \mu\text{m}$.

HAB fraction drastically increased to 40% at $L = 0.4$ mm and until the weld line, indicating a substantial increase in the recrystallization process. Therefore, this zone was identified as the weld zone. In this zone, bulging of the grain boundaries and formation of fine grains around the original grains led to the formation of a necklace structure (Fig. 15(b)). The average grain size was reduced from $40\ \mu\text{m}$ in the base material to about $4\ \mu\text{m}$ in this zone. These fine grains are characterized by a very low scatter in misorientation. Furthermore, twin boundaries, which made 34% of the grain boundaries of the base material were nearly absent in this zone with their fraction reducing to about 4% in the weld zone.

Finally, it must be noted that the observed recrystallization process was not the result of progressive movement of LAB peak toward HAB misorientations but mostly due to the building up of a wide peak near 45° , as illustrated in Fig. 16. The above observed microstructural changes correspond very well with the main characteristics of the dynamic recrystallization phenomenon, as also reported by Mironov et al. [76].

Fig. 17 shows the average grain size in the weld line of W1 (characterized with low heat input) is much larger ($20\ \mu\text{m}$) than that for W4 (characterized with high heat input) ($4\ \mu\text{m}$). This difference in grain sizes could be interpreted in terms of the influence of heat input and deformation conditions on grain size evolution and material flow at the weld interface.

The grain refinement could be associated with the occurrence of dynamic recrystallization (DRX) as described by Zener-Hollomon equations [77], $Z = \epsilon \exp\left(\frac{Q}{RT}\right)$ and $d_{DRX} = Az^{-\beta}$ where Z is the Zener-Hollomon parameter, Q activation energy for dynamic

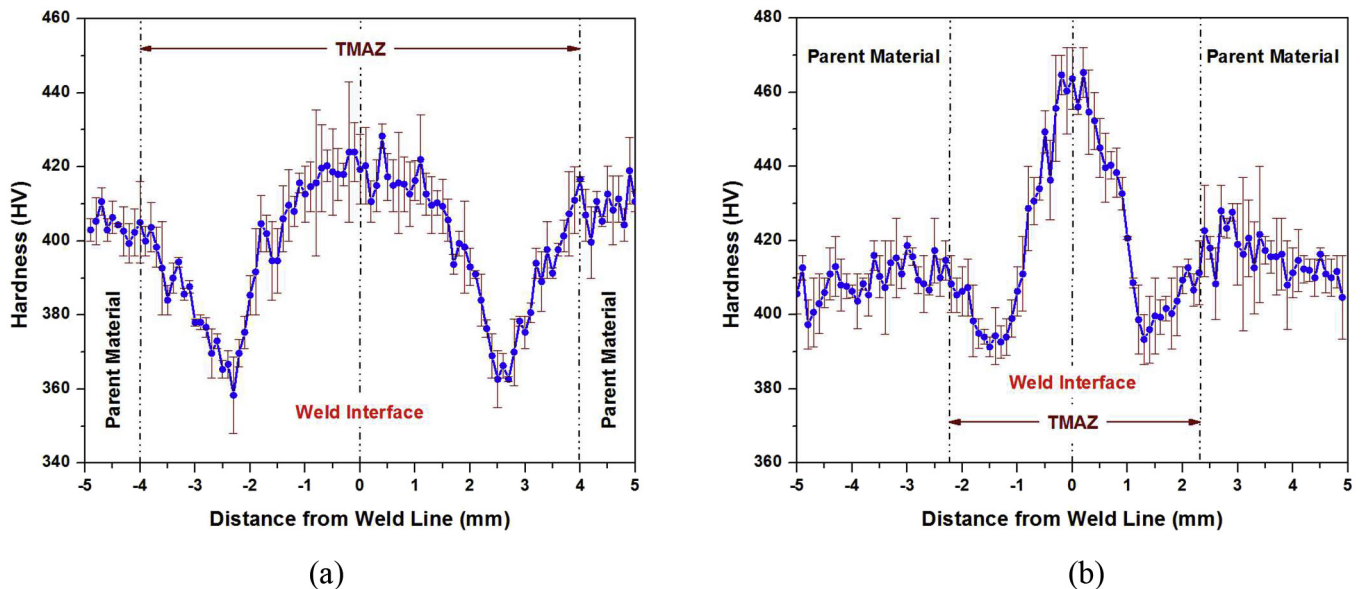


Fig. 19. Variation in microhardness with distance from the weld line of LFWed samples without PWHT produced at (a) low heat input with W1 and (b) high heat input with W4. The standard deviation of the microhardness measurement is shown by error bars.

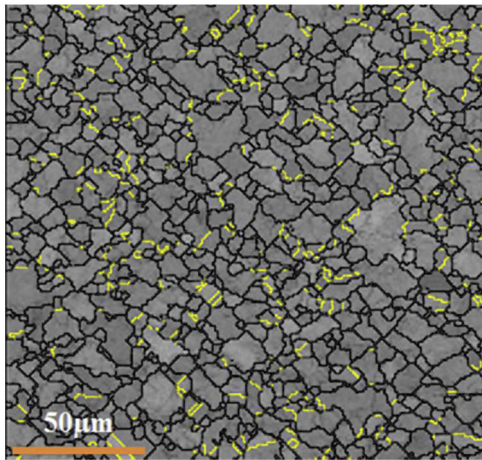


Fig. 20. EBSD grain boundary map of the LFWed W4 after PWHT.

recrystallization, ε strain rate, T temperature and A and β are material constants. According to this equation, recrystallization is accelerated at higher temperatures. As shown in Fig. 11, heat input (and consequently weld interface temperature) of W4 is higher than that of W1 (6.84×10^7 W/m² compared to 3.192×10^7 W/m²). In addition, forge pressure during LFW of W4 (580 MPa) is significantly higher than that of W1 (330 MPa). It has been reported that when the forge pressure increased from P to $2.5P$ or $4P$, DRX grain size of Waspaloy and Inconel 738 decreased from $13.1 \mu\text{m}$ to $4 \mu\text{m}$ and from $17 \mu\text{m}$ to $5 \mu\text{m}$, respectively [78,79]. Thus, lower temperature and pressure lead to lower driving force for recrystallization and consequently, bigger grain size ($20 \mu\text{m}$) in the weld line for W1, as illustrated in Fig. 17.

5.2. γ' size and volume fraction variation across the weld

In addition to changes in grain size and misorientations in different zones of the LFW joint, significant changes were also observed and quantified in volume fraction, morphology and distribution of the γ' phase. Fig. 18 shows variation of γ' size and volume fraction at different distances from the weld interface. FEG-SEM examination of the as-received AD730™ alloy revealed that the material consisted of 8% primary, 26% secondary and 3% tertiary γ' precipitates.

It must be mentioned that, X-ray diffraction could not be used to identify the precipitation of γ' phase. Indeed, since the γ - γ' lattice misfit is very small (typically of $\sim 0.1\%$ in absolute value in this class of alloys in the 600°C – 900°C and even lower at room temperature [80], γ and γ' respective peaks are overlapped in X-ray diffractograms; therefore, a clear identification of phase precipitation is very difficult.

With a decrease in distance from the weld interface, γ' precipitates volume fraction and size decreased, as shown in Fig. 18(e) and (f). Secondary and tertiary γ' precipitates began to dissolve at 2.2 mm from the interface while primary γ' particles started to dissolve from 1 mm. The total γ' volume fraction at 2.2 mm from the weld interface was similar to that of the parent material. This finding indicates that TMAZ width is around 4 to 4.4 mm which



Fig. 21. Fractured PWHT tensile samples of W4 at room temperature (RT) and 650°C .

Table 4
Room and elevated tensile properties.

Specimen	Test temperature ($^\circ\text{C}$)	Yield strength (MPa)	Ultimate tensile strength (MPa)	Elongation (%)
Base material	20	1247 ± 20	1587 ± 18	20.0 ± 3
	650	1116 ± 15	1362 ± 16	22.0 ± 3
PWHTed W4	20	1264 ± 19	1911 ± 8	22.1 ± 2
	650	1162 ± 17	1647 ± 6	24.7 ± 2
As-LFWed W4	20	961 ± 5	1781 ± 12	22.3 ± 3
	650	936 ± 7	1447 ± 10	23.2 ± 3

confirms the EBSD results shown in Figs. 13 and 14 as well as the results reported in Table 3. Furthermore, it must be emphasized that it is very difficult to fully suppress γ' precipitation on cooling from a partially/fully solutionized state. Specifically, cooling rates have to be far in excess of 100°C/s if one wants to suppress γ' precipitation [81]. The high hardness values measured in the as-welded conditions are mainly due to the combination of a refined grain size, and ultrafine γ' precipitates, typically smaller than 10 nm .

Secondary and primary γ' particles were mostly dissolved at respectively 0.8 mm , and 0.2 mm from the weld interface, as shown in Fig. 18. At the weld interface and until $100 \mu\text{m}$ away from it, all γ' precipitates were dissolved, and only a monomodal re-precipitated γ' distribution, less than 10 nm in size, was observed in the microstructure of the as-welded specimens [82]. The absence of primary or secondary γ' particles at the weld line indicates that the temperature in this zone was above the γ' solvus. Fig. 2 shows that primary γ' solvus is around 1200°C at a heating rate of 400°C/s (physically simulated heating rate at the weld interface). Therefore, the region from the weld line and until $100 \mu\text{m}$ further (i.e. very close to the weld interface) experienced temperatures higher than 1200°C which confirms the analytical results obtained from Eq. (9) for weld interface temperature.

6. Mechanical properties

6.1. Microhardness variation across the weld

Fig. 19(a) and (b) depicts the results of the microhardness measurements across the weld for W1 and W4.

It can be seen that for W1, characterized with low heat input, friction and forge pressures produced lower hardness in the weld line (425 HV) and a wider TMAZ (8.2 mm). In contrast, for W4,

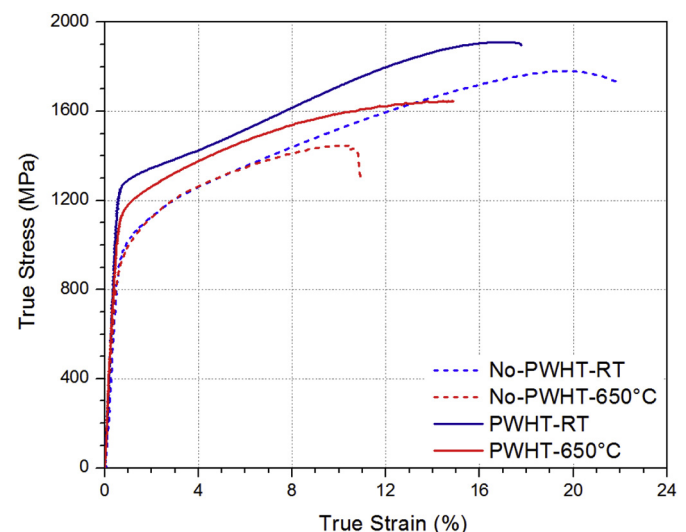


Fig. 22. Stress-strain curves of the LFWed W4 before and after heat treatment.

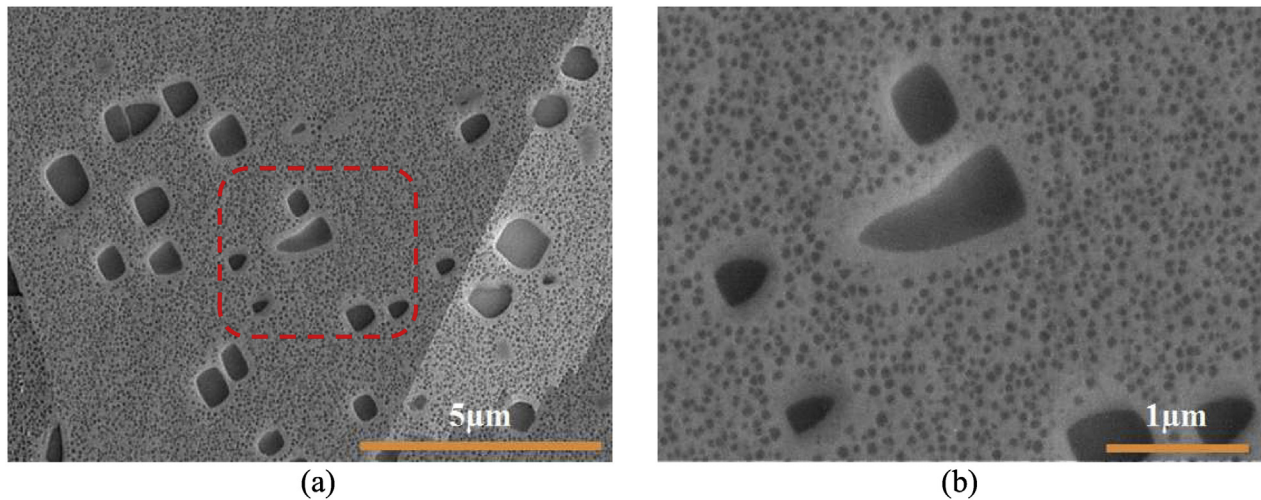


Fig. 23. FEG-SEM images γ' particles of the LFWed W4 after PWHT (a) at 1 mm from the weld interface, (b) higher magnification of the inset (red box) in (a).

characterized with high heat input, higher hardness (470 HV) and much smaller TMAZ (around 4.3 mm) were obtained. It should be noted that TMAZ is strengthened by the refined grain size at the weld line in addition to ultrafine γ' precipitates not resolved by SEM observations (size below 10 nm probably) explaining the very high hardness, even in the as-welded conditions. The lower hardness in the HAZ with and without PWHT is due to larger grain sizes (Fig. 14(a) and (b)).

The above results could be interpreted in terms of the grain sizes difference of W1 and W4. As shown in Fig. 17 the average grain size in the weld line of W1 is much larger (20 μm) than that for W4 (4 μm). Therefore, the hardness of the weld line for W1 is lower than that of W4 based on Hall-Petch equation [83]: $\sigma_y = \sigma_0 + \frac{k_y}{\sqrt{d}}$ where σ_y is the yield stress, σ_0 a material constant for the starting stress for dislocation movement, k_y the strengthening coefficient and d is the grain diameter.

Furthermore, as shown in Fig. 19(b), the width of TMAZ is

around 4.3 mm for W4 (2 to 2.2 mm on either side of the weld interface), and the size of the weld zone is 0.3–0.4 mm. These findings further confirm the EBSD and microstructure analysis results shown in Figs. 13, 14 and Table 3 for determining the size of TMAZ and weld zone.

Two symmetrically hardness zones are observed on either side of the TMAZ. At 1 mm from the weld interface, the hardness decreased from 470 to 387 HV (Fig. 19(b)). This drop in hardness can be correlated to the evolution of γ' volume fraction across the weld (Fig. 18). As shown in Fig. 18, secondary γ' volume fraction which is most effective in increasing the hardness [84] decreases from 26% in the base material to 2.9% at 1 mm from the weld interface, and lower portion of γ' particles re-precipitates compared to those of weld metal. This abrupt change is probably the root cause for the observed decrease in the microhardness level. On the other hand, Fig. 19(b) shows that with a decrease in the distance from the LFW interface, the microhardness increases gradually. This is probably

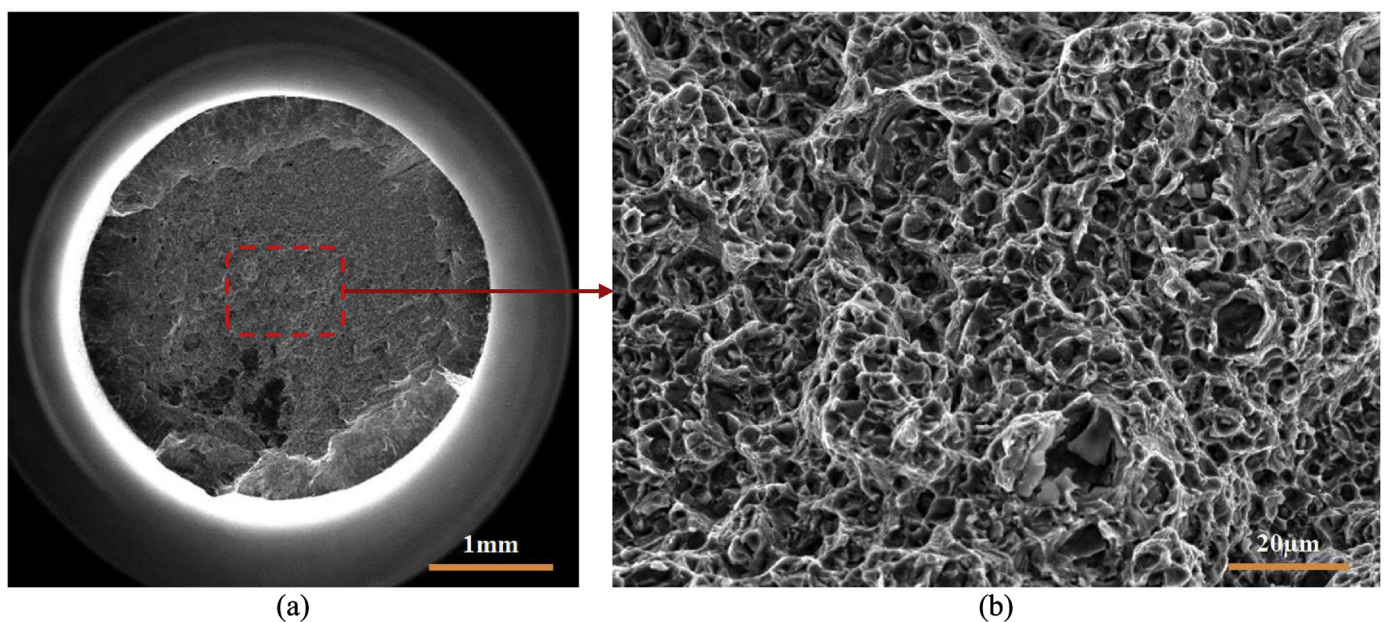


Fig. 24. (a) Macrofractograph of the fractured surface at room temperature. The central portion of the fracture is slightly flat and 45° shear lips surround this region. (b) Higher-magnification view of the selected area (red box) at the center of the specimen which consists of equiaxed dimples formed during ductile rupture.

due to γ' re-precipitation [82] and the partially refined grain structure, as shown in Fig. 14. Fig. 19(b) shows that LFW leads to significant increase in the weld hardness as the hardness of the parent material at 1 mm from the LFW interface increases from 387 to 470 HV at the weld interface. Based on Fig. 14, this increase can be attributed to grain refinement of the material, decreasing from 25 μm to 4 μm at the weld interface, during LFW and γ' re-precipitation.

Furthermore, as shown in Fig. 19, the TMAZ width in W4 is smaller than that of W1. This finding could be explained in terms of the processing conditions of W4. The higher heat input results in more heating and therefore more softening occurs in W4 compared to W1. In addition, the higher forge pressure, 580 MPa, in this sample provides more extrusion of the softened material as flash from the weld interface. The combination of these two phenomena results in smaller TMAZ width in W4. Similar trend in TMAZ reduction due to increasing forge pressure has been observed for Waspaloy and Inconel 738 [41,78].

6.2. Mechanical properties of as-welded and post weld heat treated (PWHTed) samples

As a criterion, it was considered that a defect-free and sound LFW joint was produced when its tensile strengths at room and high temperatures were higher than the ultimate tensile strength of the base material. In this case, fracture of the welded joint should appear far from the weld zone. Accordingly, the quality of the LFWed sample was evaluated by performing tensile tests at room and elevated temperatures.

It has been reported that by increasing axial shortening, the yield and ultimate tensile strengths at room temperature increase [15,41]. Therefore, in the present investigation, the weld joint with the maximum axial shortening corresponding to the highest amount of heat input (i.e. W4) was selected for evaluation. Tensile tests were conducted on as-welded and post weld heat treated samples. The average grain size in the weld interface was about 8 μm after PWHT, as shown in Fig. 20. This grain size is nearly twice

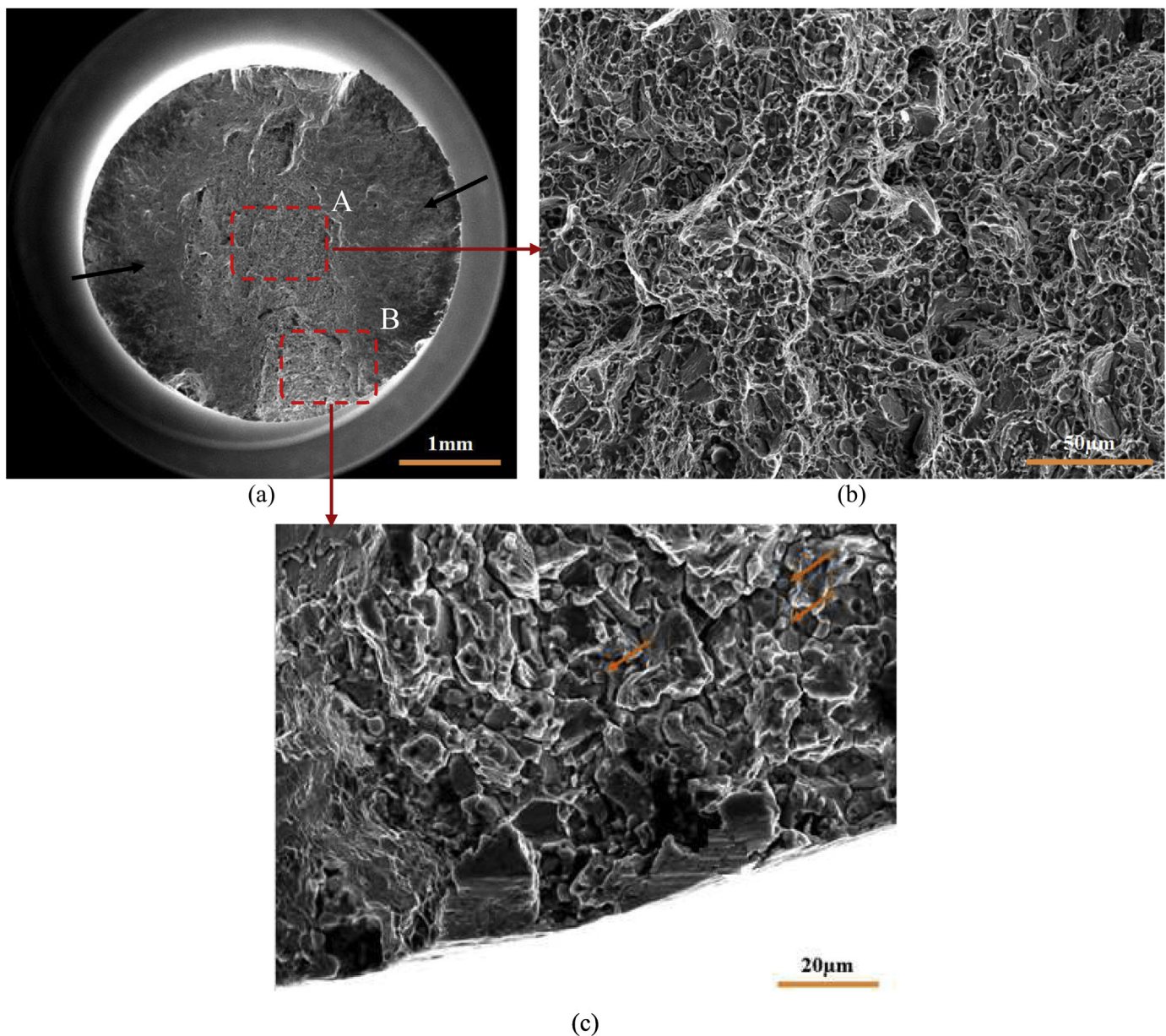


Fig. 25. (a) Macrofractograph of the fractured surface at 650 °C. Shear lips observed at 45° to the stress axis are indicated by black arrows. (b) Magnified view of a flat area from region A (inset in (a)). Ductile dimple rupture is the fracture mode. (c) Typical features of region B (inset in (a)) which consists of γ' particles (orange arrows) in the fracture surface.

the size of the grains in as welded samples. This increase could be associated with the dissolution of the primary γ' particles at the weld line, thereby facilitating the grain growth during PWHT in this zone, as demonstrated in Fig. 20.

Fractured samples after room and hot tensile tests on the PWHT W4 are shown in Fig. 21. Macroscopic examination revealed that both specimens were failed out of the weld zone. Regarding failure, the crack occurs in the region where the grain size is the largest, i.e. HAZ, due to local lower ductility, but also more slips localization due to larger grain size.

Tensile properties at room and elevated temperatures of the base material, as-LFWed joint as well as PWHT joint are given in Table 4. These data are the mean value of three tensile experiments.

Fig. 22 displays tensile stress-strain curves for LFWed samples before and after post weld heat treatment at room temperature and 650 °C. As shown in Fig. 22 and Table 4, tensile properties improved after subjecting welded specimens to post weld heat treatment. Table 4 shows that the as-welded joints have lower yield strength but higher ultimate tensile strength than those of the base material. Microstructural examination results reported in Fig. 18 showed that secondary γ' precipitates started to dissolve at 2 mm from the weld line until the weld interface, due to high temperatures experienced by this zone during LFW. On the other hand, it was found [82] that γ' particles (in the range of a few nanometers) re-precipitated in the weld interface after LFW during cooling in higher proportions than those of TMAZ [14]. Therefore, the observed higher strength of the weld zone compared to TMAZ in the present work, is probably due to higher amounts of fine γ' re-precipitation and the fine grain microstructure, as shown in Figs. 14 and 19(b). Thus, TMAZ should be the region which experiences cracking and failure during tensile tests at 650 °C of the as-welded specimens due to dissolution of strengthening precipitates and lower level of re-precipitated γ' particles.

Yield and ultimate tensile strengths of the PWHTed sample at room temperature and 650 °C show higher values than those of the base material. For example, the yield strength of the PWHTed sample tested at 650 °C is about 46 MPa higher than that of the base material. In addition, fracture strength of PWHTed sample is approximately 285 MPa more than the ultimate strength of the base material tested at 650 °C. Such behavior is indicative of forming a good joint in this sample.

The grain size in the weld region of the sample is 8 μm after PWHT which is 5 times finer than that of the base metal (40 μm). Therefore, the defect-free joint with dynamically recrystallized grains in the weld zone in this sample subjected to PWHT led to higher ultimate tensile strength. In addition, as shown in Fig. 23, PWHT leads to re-precipitation of γ' particles in the TMAZ and restores tensile properties of the LFWed joints. Thus, after PWHT, all LFWed specimens failed in the base material.

The fracture surfaces of the samples in PWHT condition were examined, and the findings are discussed in details as follows.

6.2.1. Fracture surface of tested samples in PWHT condition

The fractographic features of the tensile tested specimens at room temperature and 650 °C are shown in Figs. 24 and 25, respectively. Fig. 24 shows that the fracture surface is almost flat and dark at the center of the sample while it is bright and orientated at $\pm 45^\circ$ to the fracture surface at the edges. Higher magnification of the flat surface (Fig. 24(a)) shows dimples on fractured area, indicative of a ductile type fracture.

More detailed analysis of the fractured specimen and fracture surface (Figs. 21 and 24) revealed that failure initiated in the base material during tensile testing at room temperature. Final fracture occurred in zones adjacent to the HAZ, by shearing at $\pm 45^\circ$ to the tensile axis.

Fig. 25 shows the fracture surface of the sample tested under tensile stress at 650 °C. The surface is characterized by flat regions

of shallow dimples (Fig. 25(b)), indicative of ductile fracture. The crack propagation is transgranular, and occurs in the parent material, as shown in Fig. 25(c). The presence of primary γ' precipitates, as marked by orange arrows in Fig. 25(c), and topography of the fracture surface is consistent with an intergranular fracture, but such portions only represent a minor portion of the fracture surface. They are indicative of a possible contribution of environment (oxidation) in partially controlling failure during tensile tests at 650 °C. Two portions of the fracture surface next to the edge of the sample, shown by black arrows, are slanted suggesting a shear lip (Fig. 25(a)). Therefore, the final fracture occurs by shear, one side in the parent material and the other side in the weld zone.

In fact, one can observe from tensile tests that yielding is always lower for as welded samples compared to PWHT ones. This is mainly due to the fact that part of the γ' precipitates was solutionized during welding and did not have to fully re-precipitate during the cooling stage. Moreover, the volume fraction of γ' precipitates in the as welded condition is far from its maximum value, nor is the optimal precipitate size that maximizes the tensile properties, especially in the HAZ and close to the weld line. Finally, larger grain sizes are present in the HAZ, leading to a debit in yield stress through a lower Hall & Petch hardening effect. The results reported in Table 4 and Fig. 22 show that the yield strength is almost insensitive to the change in temperature (from room temperature to 650 °C) without PWHT, while, as expected, a decrease in tensile strength is observed when increasing the temperature to 700 °C for this alloy [46,49]. The impact of oxidation to grain boundary embrittlement or other damage mechanisms is negligible for such a short hot tensile tests at 650 °C. Indeed, the oxidation did not have enough time to affect the mechanical properties, especially tensile ductility, because tensile experiments were performed at the strain rate of 10^{-3} s^{-1} . These findings are in agreement with the results of hot tensile properties of this alloy at either higher temperature up to 850 °C [85,86] or similar Ni-based superalloys such as Udimet 720Li and RR1000 studied at lower strain rate (10^{-4} s^{-1}) [87].

7. Conclusions

- 1- An analytical method was proposed to achieve sound welds while using a minimum number of trials. The proposed method was validated by experiments, and a good agreement was obtained between the predicted axial shortening and the experiments. The analytical approach can allow for rapid determination of the optimum LFW process parameters for AD730™ alloy. The proposed methodology can be applied to other materials.
- 2- Microstructure evolution in terms of γ' size changes and dynamic recrystallization influencing mechanical properties at room and high temperatures was studied as a function of processing parameters related to ease of material flow at the weld interface.
- 3- Yield and ultimate tensile strengths of the PWHTed samples at room temperature and 650 °C showed values higher than those of the as-welded samples due to reprecipitation of γ' particles in the TMAZ indicating that a PWHT is necessary after LFW of AD730™ superalloy.
- 4- Macroscopic examination of room and high temperature PWHTed tensile samples showed that both specimens failed out of the weld zone. Tensile strengths of the PWHTed samples showed higher values than those of the base material at room temperature and 650 °C, further demonstrating the appropriate selection of processing parameters for obtaining a sound LFW joint, proposed in the present investigation.

CRedit authorship contribution statement

F. Masoumi: Conceptualization, Methodology, Investigation, Formal analysis, Visualization, Validation, Writing - original draft, Writing - review & editing. **D. Shahriari:** Conceptualization, Methodology, Data curation, Formal analysis, Software, Validation, Writing - original draft, Writing - review & editing. **H. Monajati:** Resources, Writing - review & editing. **J. Cormier:** Supervision, Funding acquisition, Resources, Validation, Writing - review & editing. **B.C.D. Flipo:** Resources, Writing - review & editing. **A. Devaux:** Resources, Writing - review & editing. **M. Jahazi:** Supervision, Funding acquisition, Resources, Validation, Writing - review & editing.

Acknowledgement

Financial support from the Natural Sciences and Engineering Research Council of Canada (NSERC) 261712 in the form of a Discovery Grant is gratefully acknowledged. The authors express appreciation to Aubert & Duval Co. for providing AD730™ samples, and to TWI Ltd. for carrying out the LFW of the samples.

References

- [1] A.R. McAndrew, P.A. Colegrove, C. Buhr, B.C.D. Flipo, A. Vairis, A literature review of Ti-6Al-4V linear friction welding, *Prog. Mater. Sci.* 92 (2018) 225–257.
- [2] A.M.M. Garcia, BLISK fabrication by linear friction welding, *Adv. Gas Turbine Technol.* (2011) 411–434.
- [3] H. Kuroki, K. Nezaki, T. Wakabayashi, K. Nakamura, Application of linear friction welding technique to aircraft engine parts, *IHI Eng. Rev.* 47 (2014) 40–43.
- [4] T.L. Bergman, A.S. Lavine, F.P. Incropera, D.P. Dewitt, *Fundamentals of Heat and Mass Transfer*, 7 Edition ed., John Wiley & Sons, 2011.
- [5] A. Chamanfar, M. Jahazi, J. Cormier, A review on inertia and linear friction welding of ni-based superalloys, *Metall. Mater. Trans. A* 46 (2015) 1639–1669.
- [6] W. Li, A. Vairis, M. Preuss, T. Ma, Linear and rotary friction welding review, *Int. Mater. Rev.* 61 (2016) 71–100.
- [7] G. Buffa, L. Fratini, Strategies for numerical simulation of linear friction welding of metals: a review, *Prod. Eng.* 11 (2017) 221–235.
- [8] M.B. Uday, M.N.A. Fauzi, H. Zuhailawati, A.B. Ismail, Advances in friction welding process: a review, *Sci. Technol. Weld. Join.* 15 (2010) 534–558.
- [9] W. Li, F. Wang, S. Shi, T. Ma, Numerical simulation of linear friction welding based on ABAQUS environment: challenges and perspectives, *J. Mater. Eng. Perform.* 23 (2014) 384–390.
- [10] M. Maalekian, Friction welding – critical assessment of literature, *Sci. Technol. Weld. Join.* 12 (2007) 738–759.
- [11] R. Turner, F. Schroeder, R.M. Ward, J.W. Brooks, The importance of materials data and modelling parameters in an FE simulation of linear friction welding, *Adv. Mater. Sci. Eng.* 2014 (2014) 1–8.
- [12] J.T. Xiong, J.L. Li, Y.N. Wei, F.S. Zhang, W.D. Huang, An analytical model of steady-state continuous drive friction welding, *Acta Mater.* 61 (2013) 1662–1675.
- [13] M. Grujicic, G. Arakere, B. Pandurangan, C.F. Yen, B.A. Cheeseman, Process modeling of Ti-6Al-4V linear friction welding (LFW), *J. Mater. Eng. Perform.* 21 (2012) 2011–2023.
- [14] F. Masoumi, D. Shahriari, M. Jahazi, J. Cormier, B.C.D. Flipo, On the occurrence of liquation during linear friction welding of Ni-based superalloys, *Metall. Mater. Trans. A* 48 (2017) 2886–2899.
- [15] P. Wanjara, M. Jahazi, Linear friction welding of Ti-6Al-4V: processing, microstructure, and mechanical-property inter-relationships, *Metall. Mater. Trans. A* 36 (2005) 2149–2164.
- [16] M. Smith, J.B. Levesque, L. Bichler, D. Sediako, J. Gholipour, P. Wanjara, Residual stress analysis in linear friction welded in-service Inconel 718 superalloy via neutron diffraction and contour method approaches, *Mater. Sci. Eng. A* 691 (2017) 168–179.
- [17] M. Preuss, P.J. Withers, J.W.L. Pang, G.J. Baxter, Inertia welding nickel-based superalloy: part I. Metallurgical characterization, *Metall. Mater. Trans. A* 33 (2002) 3215–3225.
- [18] M. Preuss, P.J. Withers, J.W.L. Pang, G.J. Baxter, Inertia welding nickel-based superalloy: part II. Residual stress characterization, *Metall. Mater. Trans. A* 33 (2002) 3227–3234.
- [19] P. Jedrasiak, H.R. Shercliff, Modelling of heat generation in linear friction welding using a small strain finite element method, *Mater. Des.* 177 (2019), 107833.
- [20] G. Qin, P. Geng, J. Zhou, Z. Zou, Modeling of thermo-mechanical coupling in linear friction welding of Ni-based superalloy, *Mater. Des.* 172 (2019), 107766.
- [21] P. Li, J. Li, H. Dong, Analytical description of heat generation and temperature field during the initial stage of rotary friction welding, *J. Manuf. Process.* 25 (2017) 181–184.
- [22] J.T. Xiong, L. Yuan, Y.J. Du, J.M. Shi, J.L. Li, The thermodynamic analytical models for steady-state of continuous drive friction welding based on the maximum entropy production principle, *Appl. Therm. Eng.* 159 (2019), 113840.
- [23] M.R. Kelly, S.R. Schmid, D.C. Adams, J. Fletcher, R. Heard, Experimental investigation of linear friction welding of AISI 1020 steel with pre-heating, *J. Manuf. Process.* 39 (2019) 26–39.
- [24] R.C. Reed, *The Superalloys Fundamentals and Applications*, Cambridge University Press, 2006.
- [25] J. Donachie Matthew, J. Donachie Stephen, *Superalloys-A Technical Guide*, 2nd Edition, ASM International; ASM International, 2002.
- [26] A. Thomas, M. El-Wahabi, J.M. Cabrera, J.M. Prado, High temperature deformation of Inconel 718, *J. Mater. Process. Technol.* 177 (2006) 469–472.
- [27] S. Mahadevan, S. Nalawade, J.B. Singh, A. Verma, B. Paul, K. Ramaswamy, Evolution of δ phase microstructure in alloy 718, in: 7th International Symposium on Superalloy 718 and Derivatives, Pittsburgh, PA, United States, 10–13 October, 2010, pp. 737–750.
- [28] C. Mary, M. Jahazi, Linear friction welding of IN-718 process optimization and microstructure evolution, in: 5th International Conference on Processing and Manufacturing of Advanced Materials - THERMEC 2006, 4–8 July, Vancouver, BC, Canada, 2006, pp. 357–362.
- [29] N. Iqbal, J. Rolph, R. Moat, D. Hughes, M. Hofmann, J. Kelleher, G. Baxter, P.J. Withers, M. Preuss, A comparison of residual stress development in inertia friction welded fine grain and coarse grain nickel-base superalloy, *Metall. Mater. Trans. A* 42 (2011) 4056–4063.
- [30] F. Masoumi, M. Jahazi, D. Shahriari, J. Cormier, Coarsening and dissolution of γ' precipitates during solution treatment of AD730™ Ni-based superalloy: mechanisms and kinetics models, *J. Alloys Compd.* 658 (2016) 981–995.
- [31] F. Masoumi, D. Shahriari, M. Jahazi, J. Cormier, A. Devaux, Kinetics and mechanisms of γ' reprecipitation in a Ni-based superalloy, *Sci. Rep.* 6 (2016), 28650.
- [32] J. Cormier, G. Cailletaud, Constitutive modeling of the creep behavior of single crystal superalloys under non-isothermal conditions inducing phase transformations, *Mater. Sci. Eng. A* 527 (2010) 6300–6312.
- [33] J. Cormier, X. Milhet, J. Mendez, Non-isothermal creep at very high temperature of the nickel-based single crystal superalloy MC2, *Acta Mater.* 55 (2007) 6250–6259.
- [34] J.B. le Graverend, J. Cormier, M. Jouiad, F. Gallerneau, P. Paulmier, F. Hamon, Effect of fine γ' precipitation on non-isothermal creep and creep-fatigue behaviour of nickel base superalloy MC2, *Mater. Sci. Eng. A* 527 (2010) 5295–5302.
- [35] G.B. Viswanathan, R. Shi, A. Genc, V.A. Vorontsov, L. Kovarik, C.M.F. Rae, M.J. Mills, Segregation at stacking faults within the γ' phase of two Ni-base superalloys following intermediate temperature creep, *Scr. Mater.* 94 (2015) 5–8.
- [36] O.T. Ola, O.A. Ojo, M.C. Chaturvedi, Effect of deformation mode on hot ductility of a γ' precipitation strengthened nickel-base superalloy, *Mater. Sci. Eng. A* 585 (2013) 319–325.
- [37] D. Shahriari, M.H. Sadeghi, A. Akbarzadeh, M. Cheraghzadeh, The influence of heat treatment and hot deformation conditions on γ' precipitate dissolution of nimonic 115 superalloy, *Int. J. Adv. Manuf. Technol.* 45 (2009) 841–850.
- [38] J. Wang, J. Dong, M. Zhang, X. Xie, Hot working characteristics of nickel-base superalloy 740H during compression, *Mater. Sci. Eng. A* 566 (2013) 61–70.
- [39] Y. Wang, W.Z. Shao, L. Zhen, B.Y. Zhang, Hot deformation behavior of delta-processed superalloy 718, *Mater. Sci. Eng. A* 528 (2011) 3218–3227.
- [40] R. Damodaram, S. Ganesh Sundara Raman, K. Prasad Rao, Effect of post-weld heat treatments on microstructure and mechanical properties of friction welded alloy 718 joints, *Mater. Des.* 53 (2014) 954–961.
- [41] A. Chamanfar, M. Jahazi, J. Gholipour, P. Wanjara, S. Yue, Maximizing the integrity of linear friction welded Waspaloy, *Mater. Sci. Eng. A* 555 (2012) 117–130.
- [42] F. Daus, H. Li, G. Baxter, S. Bray, P. Bowen, Mechanical and microstructural assessment of RR1000 to IN718 inertial welds-effects of welding parameters, *Mater. Sci. Technol.* 23 (2007) 1424–1432.
- [43] M. Preuss, P.J. Withers, G. Baxter, A comparison of inertia friction welds in three nickel base superalloys, *Mater. Sci. Eng. A* 437 (2006) 38–45.
- [44] Z.W. Huang, H.Y. Li, M. Preuss, M. Karadge, P. Bowen, S. Bray, G. Baxter, Inertia friction welding dissimilar nickel-based superalloys Alloy 720Li to IN718, *Metall. Mater. Trans. A* 38 (2007) 1608–1620.
- [45] O.T. Ola, O.A. Ojo, P. Wanjara, M.C. Chaturvedi, Analysis of microstructural changes induced by linear friction welding in a nickel-base superalloy, *Metall. Mater. Trans. A* 42 (2011) 3761–3777.
- [46] A. Devaux, B. Picque, M.F. Gervais, E. Georges, T. Poulain, P. Héritier, AD730™-a new nickel-based superalloy for high temperature engine rotative parts, in: 12th International Symposium on Superalloys, Superalloys 2012, Seven Springs, PA, United States, 9–13 September, 2012, pp. 911–919.
- [47] A. Devaux, A. Helstroffer, J. Cormier, P. Villechaise, J. Douin, M. Hantcherli, F. Pettinari-Sturmel, Effect of aging heat-treatment on mechanical properties of AD730™ superalloy, in: 8th International Symposium on Superalloy 718 and Derivatives, 2014, Pittsburgh, PA, United States, 28 September–1 October, 2014, pp. 521–535.
- [48] A. Devaux, E. Georges, P. Héritier, Properties of new C&W superalloys for high temperature disk applications, Superalloy 718 and Derivatives, in: 7th International Symposium on Superalloy 718 and Derivatives, 2010, Pittsburgh, PA,

- United States, 10–13 October, 2010, pp. 223–235.
- [49] A. Devaux, L. Berglin, L. Thébaud, R. Delattre, C. Crozet, O. Nodin, Mechanical properties and development of supersolvus heat treated new nickel base superalloy AD730™, in: MATEC Web of Conferences 14, 2014, p. 01004.
- [50] C. Bellot, P. Lamesle, Quantitative measurement of gamma prime precipitates in two industrial nickel-based superalloys using extraction and high resolution SEM imaging, *J. Alloys Compd.* 570 (2013) 100–103.
- [51] T. Altan, G. Ngaile, G. Shen, *Cold and Hot Forging: Fundamentals and Applications*, ASM International, 2005.
- [52] G.E. Dieter, H.A. Kuhn, S.L. Semiatin, *Handbook of Workability and Process Design*: ASM International, Materials Park, Ohio, USA, 2003.
- [53] W.F. Hosford, R.M. Caddell, *Metal Forming: Mechanics and Metallurgy*, Cambridge University Press, 2014.
- [54] Y.C. Lin, X.M. Chen, A critical review of experimental results and constitutive descriptions for metals and alloys in hot working, *Mater. Des.* 32 (2011) 1733–1759.
- [55] U.S. Dixit, S.N. Joshi, J.P. Davim, Incorporation of material behavior in modeling of metal forming and machining processes: a review, *Mater. Des.* 32 (2011) 3655–3670.
- [56] X. Yang, W. Li, J.L. Li, B. Xiao, T. Ma, Z. Huang, J. Guo, Finite element modeling of the linear friction welding of GH4169 superalloy, *Mater. Des.* 87 (2015) 215–230.
- [57] P. Geng, G. Qin, L. Chen, J. Zhou, Z. Zou, Simulation of plastic flow driven by periodically alternating pressure and related deformation mechanism in linear friction welding, *Mater. Des.* 178 (2019), 107863.
- [58] P. Geng, G. Qin, J. Zhou, Z. Zou, Finite element models of friction behaviour in linear friction welding of a Ni-based superalloy, *Int. J. Mech. Sci.* 152 (2019) 420–431.
- [59] X. Yang, W. Li, J. Ma, S. Hu, Y. He, L. Li, B. Xiao, Thermo-physical simulation of the compression testing for constitutive modeling of GH4169 superalloy during linear friction welding, *J. Alloys Compd.* 656 (2016) 395–407.
- [60] H. Jiang, J. Dong, M. Zhang, L. Zheng, Z. Yao, Hot deformation characteristics of alloy 617B nickel-based superalloy: a study using processing map, *J. Alloys Compd.* 647 (2015) 338–350.
- [61] H. Jiang, J. Dong, M. Zhang, Z. Yao, A study on the effect of strain rate on the dynamic recrystallization mechanism of alloy 617B, *Metall. Mater. Trans. A* 47 (2016) 5071–5087.
- [62] H. Jiang, J. Dong, M. Zhang, Z. Yao, Phenomenological model for the effect of strain rate on recrystallization and grain growth kinetics in the 617B alloy, *J. Alloys Compd.* 735 (2018) 1520–1535.
- [63] Y.C. Lin, D.-X. Wen, J. Deng, G. Liu, J. Chen, Constitutive models for high-temperature flow behaviors of a Ni-based superalloy, *Mater. Des.* 59 (2014) 115–123.
- [64] F. Chen, J. Liu, H. Ou, B. Lu, Z. Cui, H. Long, Flow characteristics and intrinsic workability of IN718 superalloy, *Mater. Sci. Eng. A* 642 (2015) 279–287.
- [65] R. Turner, J.C. Gebelin, R.M. Ward, R.C. Reed, Linear friction welding of Ti–6Al–4V: modelling and validation, *Acta Mater.* 59 (2011) 3792–3803.
- [66] A. Vairis, G. Papazafeiropoulos, A.M. Tsainis, A comparison between friction stir welding, linear friction welding and rotary friction welding, *Adv. Manuf.* 4 (2016) 296–304.
- [67] O.T. Ola, O. Ojo, P. Wanjara, M. Chaturvedi, Crack-free welding of IN 738 by linear friction welding, in: *Euro Superalloys 2010, 2011*, pp. 446–453.
- [68] A.C. Addison, Linear friction welding information for production engineering, in: *TWI Industrial Members Report — 961/2010, 2010*. U.K; Cambridge.
- [69] A. Vairis, M. Frost, On the extrusion stage of linear friction welding of Ti 6Al 4V, *Mater. Sci. Eng. A* 271 (1999) 477–484.
- [70] B.S. Yilbas, A.Z. Sahin, *Friction Welding: Thermal and Metallurgical Characteristics*, Springer Science & Business Media, 2014.
- [71] T.L. Bergman, F.P. Incropera, *Fundamentals of Heat and Mass Transfer*, John Wiley & Sons, 2011.
- [72] L.E. Lindgren, Numerical modelling of welding, *Comput. Methods Appl. Mech. Eng.* 195 (2006) 6710–6736.
- [73] O. Grong, *Metallurgical Modelling of Welding*, Second Edition ed, Institute of Materials, 1997.
- [74] O.N. Senkov, D.W. Mahaffey, S.L. Semiatin, C. Woodward, Inertia friction welding of dissimilar superalloys Mar-M247 and LSHR, *Metall. Mater. Trans. A* 45 (2014) 5545–5561.
- [75] S.Y. Mironov, G.A. Salishchev, M.M. Myshlyaev, R. Pippin, Evolution of misorientation distribution during warm 'abc' forging of commercial-purity titanium, *Mater. Sci. Eng. A* 418 (2006) 257–267.
- [76] S. Mironov, Y. Zhang, Y.S. Sato, H. Kokawa, Development of grain structure in β -phase field during friction stir welding of Ti–6Al–4V alloy, *Scr. Mater.* 59 (2008) 27–30.
- [77] S.C. Medeiros, Y.V.R.K. Prasad, W.G. Frazier, R. Srinivasan, Microstructural modeling of metadynamic recrystallization in hot working of IN 718 superalloy, *Mater. Sci. Eng. A* 293 (2000) 198–207.
- [78] M.Y. Amegadzie, Effect of Forging Pressure on the Microstructure of Linear Friction Welded Inconel 738 Superalloy, Department of Mechanical and Manufacturing Engineering, University of Manitoba, Canada; Master of Science, 2012.
- [79] A. Chamanfar, M. Jahazi, J. Gholipour, P. Wanjara, S. Yue, Modeling grain size and strain rate in linear friction welded Waspaloy, *Metall. Mater. Trans. A* 44 (2013) 4230–4238.
- [80] D.M. Collins, L. Yan, E.A. Marquis, L.D. Connor, J.J. Ciardiello, A.D. Evans, H.J. Stone, Lattice misfit during ageing of a polycrystalline nickel-base superalloy, *Acta Mater.* 61 (2013) 7791–7804.
- [81] T. Grosdidier, A. Hazotte, A. Simon, Precipitation and dissolution processes in γ/γ' single crystal nickel-based superalloys, *Mater. Sci. Eng. A* 256 (1998) 183–196.
- [82] F. Masoumi, L. Thébaud, D. Shahriari, M. Jahazi, J. Cormier, A. Devaux, B.C.D. Flipo, High temperature creep properties of a linear friction welded newly developed wrought Ni-based superalloy, *Mater. Sci. Eng. A* 710 (2018) 214–226.
- [83] W.D. Callister Jr., D.G. Rethwisch, *Fundamental of Materials Science and Engineering: An Integrated Approach*, John Wiley & Sons, 2012.
- [84] H. Monajati, M. Jahazi, R. Bahrami, S. Yue, The influence of heat treatment conditions on γ' characteristics in Udimet® 720, *Mater. Sci. Eng. A* 373 (2004) 286–293.
- [85] L. Thébaud, P. Villechaise, J. Cormier, C. Crozet, A. Devaux, D. Béchet, J.-M. Franchet, A. Organista, F. Hamon, Relationships between microstructural parameters and time-dependent mechanical properties of a new nickel-based superalloy AD730™, *Metals* 5 (2015) 2236–2251.
- [86] L. Thébaud, P. Villechaise, C. Crozet, A. Devaux, D. Béchet, J.-M. Franchet, A.-L. Rouffié, M. Mills, J. Cormier, Is there an optimal grain size for creep resistance in Ni-based disk superalloys? *Mater. Sci. Eng. A* 716 (2018) 247–283.
- [87] A.A.N. Németh, D.J. Crudden, D.E.J. Armstrong, D.M. Collins, K. Li, A.J. Wilkinson, C.R.M. Grovenor, R.C. Reed, Environmentally-assisted grain boundary attack as a mechanism of embrittlement in a nickel-based superalloy, *Acta Mater.* 126 (2017) 361–371.